THESIS FOR THE DEGREE OF DOCTOR OF PHOLOSOPHY

Characterisation of a structural battery composite and its constituents

SHANGHONG DUAN

Department of Industrial and Materials Science

Division of Material and Computational Mechanics

CHALMERS UNIVERISTY OF TECHNOLOGY

Gothenburg, Sweden 2022

Characterisation of a structural battery composite and its constituents

SHANGHONG DUAN

ISBN 978-91-7905-730-5

Doktorsavhandlingar vid Chalmers tekniska högskola
Ny serie nr. 5196
ISSN 0346-718X

Department of Industrial and Materials Science
Division of Material and Computational Mechanics
Chalmers University of Technology
SE-412 96 Gothenburg
Sweden
Telephone: +46 (0)31-772 1000

Cover:

Schematic illustration of Schematic illustration of a structural battery and characterisation works of its constituents in this thesis.

Chalmers Reproservice

Gothenburg, Sweden 2022

Characterisation of a structural battery composite and its constituents

Shanghong Duan
Department of Industrial and Materials Science
Division of Material and Computational Mechanics
Chalmers University of Technology

Abstract

The structural battery composite is a recently successfully developed multifunctional lithium-ion battery. It is safer and capable to carry mechanical load compared to commercially available liquid electrolyte batteries. This makes it possible to apply the structural batteries to replace parts of the structural components in a system and thus reduce the weight of the whole system. The structural battery composite uses carbon fibre, an excellent lightweight material, as the anode material and uses a semi-solid structural battery electrolyte (SBE) material. The entire battery behaves as a solid material. The overall mechanical properties of the structural battery composite material are excellent due to the reinforcement of the carbon fibres and the mechanically robust SBE matrix.

In this thesis, first of all, a multifunctional structural battery composite is manufactured. The structural battery composite uses the lithium storage capacity of carbon fibre for the first time and therefore, has an energy density of 24 Wh/kg and an elastic modulus of 25 GPa. Secondly, characterisation methods were developed for a number of important components in the structural battery composite. This includes precise measurements of transverse and shear moduli on micron-scale carbon fibres, the effect of lithiation on the carbon fibre anode mechanical properties, and 3D reconstruction and simulation of the SBE. For the pristine carbon fibres, focused ion beam combined with scanning electron microscopy (FIB/SEM) was used to accurately mill flat surfaces in different orientations on the carbon fibres, followed by indentation test using atomic force microscopy, and nanoindentation. The elastic hysteresis of the carbon fibres was observed in the experiments. For the first time, the moduli in the transverse and shear directions were derived in conjunction with an accurate orthotropic mechanical model. For the study of lithiation effects on the carbon fibre anode, the focus is on volume expansion and modulus changes. The volume expansion was obtained by analysis of SEM and optical micrographs. By using the protection of hydrophobic ionic liquids, the samples were successfully transferred into a vacuum environment in the SEM and subjected to transverse compression experiments. The transverse modulus of the carbon fibres is found to be doubled after lithiation. Finally, the microstructure of the SBE was reconstructed in 3D. The geodesic tortuosity of the SBE was found to be approximately 1.8. Meanwhile, the elastic modulus and ionic conductivity of the SBE were experimentally measured and simulated. In terms of elastic modulus, the results were consistent, and in terms of ionic conductivity, the simulated result overestimated the measured result.

Keywords: biomimetic, structural battery, lithiation, carbon fibres, structural battery electrolyte, characterisation, elastic modulus, volume expansion, 3D reconstruction.

Preface

The present work was performed from December 2017 to November 2022 at the Division of Material and Computational Mechanics, Department of Industrial and Materials science, Chalmers University of Technology. The project is funded by the European Union, Clean Sky Joint Undertaking 2, Horizon 2020 under Grant Agreement Number 738085, USAF, contract FA9550-17-1-0338, USAF, EOARD Award No. FA8655-21-1-7038, ONR, USA, Award No. N62909-22-1-2037 and the Swedish National Space Agency, project no. 2020-00256.

Acknowledgements

As my 5-year PhD journey comes to an end, this period of study and research will be one of the most precious memories of my life. When I first applied for my PhD position, I was still majored in metallic materials. During these years I have had an opportunity to gain a wide range of knowledge of different areas such as batteries, carbon fibres, mechanics and materials characterisation methods. In the course of the PhD studies, I have been assisted by many people.

First of all, I would like to express my sincere gratitude to my supervisor, Professor Leif Asp. It was he who gave me this precious opportunity of the PhD journey. His guidance in research directions, extensive knowledge and selfless support have all made the PhD journey easier. His rigorous research attitude and patience were key to our success, especially in the first few years when our structural battery failed a lot. Leif is always active in advising and providing all his help. He is an excellent mentor, and I am lucky to work with him.

Secondly, I would like to thank my co-supervisor, Associate Professor Fang Liu. Her in-depth knowledge and skills in electron microscopy helped and taught me a lot. She was always happy and patient for discussions when needed. Thanks for her compassionate help in making all the work possible. The time spent with Fang at Lab was always relaxed and joyful.

Moreover, I would like to thank my colleagues and friends in the division of Material and Computational Mechanics at Chalmers, especially David Carlstedt, Johanna Xu and Marcus Johansen from the structural battery group, with whom discussions and research were always fun. I would also like to thank the structural battery group at KTH Royal Institute of Technology for their generous knowledge sharing and discussions.

Finally, I would like to thank my beloved girlfriend Yuyin Jin. Her company and encouragement have given me the motivation to move forward. Thank you for your willingness to listen to my work. You make my life outside of work rich and meaningful.

The papers included in this thesis:

Paper A **A structural battery and its multifunctional performance**

L.E Asp, K. Bouton, D. Carlstedt, **S. Duan**, R. Harnden, W. Johannisson, M. Johansen, M. KG Johansson, G. Lindbergh, F. Liu, K. Peuvot, L. M. Schneider, J. Xu, D. Zenkert,

Published in *Advanced Energy and Sustainability Research* 2021, 2.

Paper B **Transverse modulus measurement of carbon fibre by atomic force microscope and nanoindentation**

S. Duan, F. Liu, T. Pettersson, C. Creighton, L.E. Asp,

Proceedings of the 22nd International Conference on Composite Materials.

Paper C **Determination of transverse and shear moduli of single carbon fibres**

S. Duan, F. Liu, T. Pettersson, C. Creighton, L.E. Asp,

Published in *Carbon* 2020, 158.

Paper D **Effect of lithiation on the elastic moduli of carbon fibres**

S. Duan, A.H.S. Iyer, D. Carlstedt, F. Rittweger, A. Sharits, C. Maddox, K.-R. Riemschneider, D. Mollenhauer, M. Colliander, F. Liu, L.E. Asp,

Published in *Carbon* 2021, 185.

Paper E **3D reconstruction and computational analysis of a structural battery composite porous electrolyte**

S. Duan, M. Cattaruzza, V. Tu, R. Auenhammer, M. Johansson, F. Liu, L.E. Asp,

Submitted.

In paper A, the author of the thesis was responsible for study of one type of structural battery, microscopy work, and writing parts of the original draft. In papers B and C, the author did major work including all experiments excluded nanoindentation, data analysis, model development, and wrote the original draft. In paper D, the author studied and designed the experiments, prepared the specimen, preformed microscopy work, data analysis and wrote the original draft. In paper E, the author did the microscopy work, reconstructed the 3D model and wrote the original draft.

Papers not included in the thesis:

F. Liu, S. Duan, L.E. Asp, Specimen preparation for transverse modulus measurement of carbon fibres using focused ion beam, Proceedings of 22nd International Conference of Composite Materials (ICCM22), Melbourne, AUS, 2019.

D. Carlstedt, F. Rittweger, K. Runesson, A.M. Navarro-Suárez, J. Xu, S. Duan, F. Larsson, K.-R. Riemschneider, L.E Asp, Experimental and computational characterization of carbon fibre based structural battery electrode laminae, *Composites Science and Technology*, 2022, 220, 109283.

J. Xu, Z. Geng, M. Johansen, D. Carlstedt, S. Duan, T. Thiringer, F. Liu, L.E. Asp, A multicell structural battery composite laminate, *EcoMat*, 2022, 4, e12180.

S. Duan, F. Lindelöw, Z. Li, Z. Ma, Y. Liu, J. Xu, D. Carlstedt, M. Johansen, L.E. Asp, Building and characterization of symmetric structural battery, Proceedings of the 20th European Conference on Composite Materials, ECCM20.

Content

1 Introduction

Clean energy technologies have gained a great deal of attention and development in recent years. Rechargeable batteries, represented by lithium-ion batteries, are widely used [1]. The most common example is the electric vehicle. As an important component of an electric vehicle, the performance of the battery, such as weight, energy density and safety, has a direct impact on the final vehicle performance. The most common lithium-ion batteries consist of a lithium intercalated oxide cathode, a graphite anode and a liquid organic electrolyte.

The lithium ions have different chemical potentials in the anode and cathode. When the lithium-ion battery is charged, the lithium ions are extracted from the cathode, where the lithium ions have a lower chemical potential, and move to the anode, where higher chemical potential energy is obtained. At the same time, electrons flow from the cathode to the anode through an external circuit. During the discharge process, the lithium ions spontaneously flow from the higher chemical potential anode to the lower chemical potential cathode. This energy storage process is similar to reservoir energy storage where water is pumped from a lower position to a higher position in order to generate electricity by opening the floodgates when needed. In such a device, it is necessary to ensure that the electrolyte is ion-conductive but electrically insulating and the anode and cathode are not in contact to avoid internal short circuits. The lithium-ion battery is schematically illustrated in Figure 1.

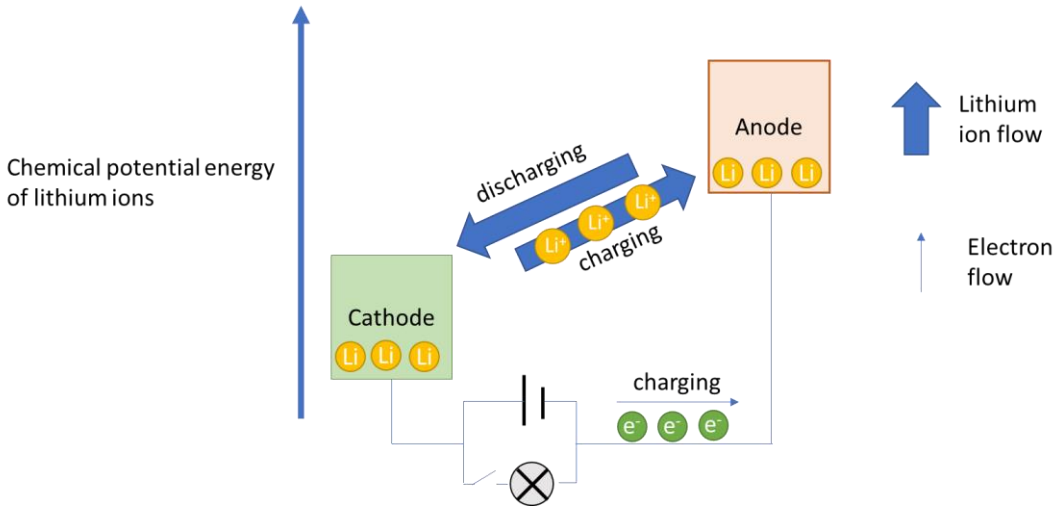

Figure 1. Schematic of lithium-ion battery. A charging process of the ion and electron currents is shown.

The current challenge for lithium-ion batteries is to increase energy density and safety [1]. The main methods of increasing energy density are focused on the development of high energy density anode and cathode materials, and the use of ultra-thin separator. Among the different anode materials, lithium metal and silicon both have a much higher energy density than graphite. However, the use of lithium metal is limited by the safety issues associated with dendrite growth [2]. Silicon electrodes, on the other hand, are limited by the near 400 % volume expansion [3]. Among the cathode materials, ternary metal oxide has a higher energy density [4]. Similarly, it is less safe than lithium iron phosphate electrodes, which have a lower energy density. It can be seen that energy density and safety are usually traded off against each other. In order to improve the safety of batteries, the solid-state battery has received the most attention [5,6]. Since the main safety concerns for batteries are internal short circuits and the flammability of the liquid electrolyte, the use of solid-state electrolytes in solid-state batteries can solve both issues simultaneously. To increase the energy density of the battery and at the same time ensure the safety of the battery, structural batteries are proposed as a novel solution [6,7,8,9,10].

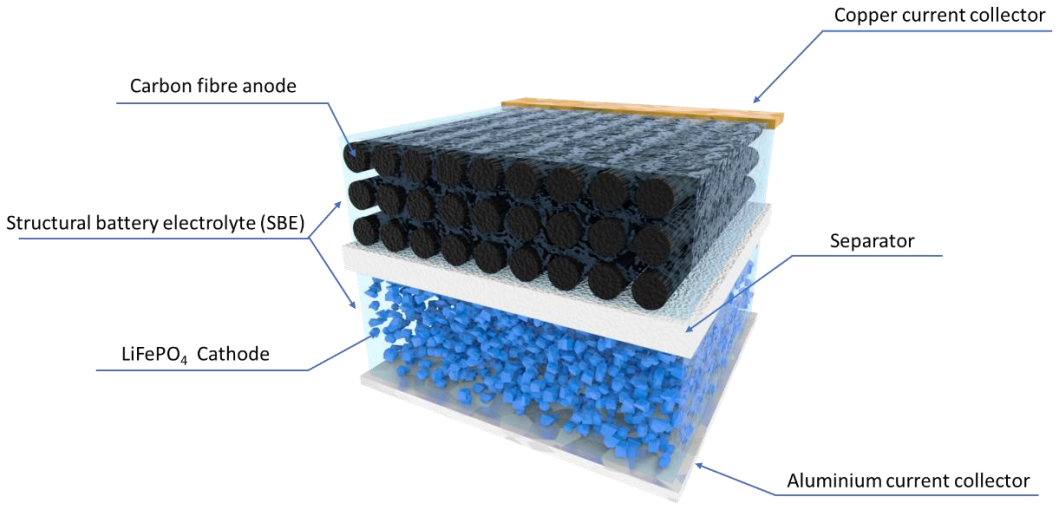

Figure 2. Schematic diagram of the concept of a structural battery

Structural batteries can be seen as solid-state batteries using carbon fibre as the anode material. A schematic structure of a structural battery composite is presented in Figure 2. As a representative material for lightweight application, carbon fibre has excellent mechanical properties and high chemical stability [11]. Its specific modulus and specific strength in fibre direction are approximately 6 to 10 times higher than those of metallic materials [12]. The carbon fibre reinforced polymer composite is a widely used lightweight composite material. The atomic structure of carbon fibres is very similar to that of graphite, possessing stacking of graphene layered structure linked by van der Waals attraction. The structure is an important reason why graphite can be used as an excellent electrode material. The structural similarity makes carbon fibre and graphite similar in their electrochemical properties. Kjell et al. used carbon fibres in liquid electrolyte lithium-ion batteries and obtained good energy density [13]. In structural batteries, the energy density of the electrode material is not increased. Consequently, there are no safety issues arising from the use of the carbon fibre anode. In addition, the solid/semi-solid electrolyte in the structural battery composite is safer than the liquid electrolyte in commercial lithium-ion batteries. In fact, the biggest advantage of using a carbon fibre anode is that it gives the battery sufficient mechanical properties to carry mechanical load. This means that when using a structural battery composite as an energy source in, e.g., an electric vehicle, part of the structural components can be replaced. The weight of the whole system is then reduced. Some studies have shown that by using structural batteries,

the weight of an electric vehicle can be reduced by up to 30 %, resulting in a 70 % increase in mileage [14]. The “high energy density” of structural batteries therefore comes from the use of their mechanical properties to reduce the weight of the whole system.

The multifunctionality of structural batteries is attractive but complex. Both the electrochemical and mechanical properties of the structural battery composite are utilised. The different materials must be matched to ensure a balanced battery cell and mechanical load transfer and to avoid any undesired chemical reactions. This requires, above all, a good knowledge of the individual materials used. This includes their electrochemical properties, mechanical properties and the coupling effects between the electrochemistry and mechanics. The most important materials in the structural battery composite are the carbon fibre anode and the semi-solid electrolyte as they are the main sources of the excellent mechanical properties of the structural battery composite. The characterisation of the electrochemical properties of the materials is not complicated and the traditional electrochemical characterisation methods of battery materials are still applicable; for example, the measurement of the energy density of electrode materials by battery cycling and the measurement of the ionic conductivity of the electrolyte by electrochemical impedance spectroscopy. Due to the existence of the coupling effects, the mechanical properties of the carbon fibre anode associated with electrochemistry must also be well characterised. However, due to the high activity and small size of the battery material constituents, there are no suitable methods available for their characterisation.

Scope of the thesis

In the thesis we focus on the fabrication of structural batteries and the studies of material characterisation methods for structural battery constituents. Measurements of the mechanical properties of carbon fibre anodes and the coupling effects of their mechanical properties to the state of lithiation (SOC) are in focus. Three-dimensional (3D) reconstruction, analysis, and simulation of the porous structure of the structural battery electrolyte (SBE) is also pursued. Specific research topics are as follows:

Paper A Fabrication and characterisation of a structural battery. This is the first structural battery to use carbon fibre directly as an anode material. The battery demonstrates a good compromise of the mechanical and electrochemical properties.

Papers B and C investigate the experimental method for measuring the elastic moduli of carbon fibres in different directions. By using the focused ion beam (FIB) technique, flat surfaces are precisely milled on the carbon fibre. The indentation modulus is measured in two different directions and combined with an elastic contact model of the orthotropic material to derive the moduli of the carbon fibre in the transverse and longitudinal directions.

Paper D characterises the effects of the lithiation on carbon fibres, including transverse modulus and volume expansion measurements. Due to the small size and high activity of the lithiated carbon fibre in air, ionic liquid is selected to cover and protect the sample during the transportation into the scanning electron microscope (SEM), where transverse compression experiments were performed in a vacuum environment.

Paper E 3D reconstructions, simulation of the porous SBE. Milled surface images of SBE were obtained using FIB-SEM technique, post-processed using commercial software. 3D models were generated. The 3D models were analysed to obtain the pore size, distribution, connectivity, and geodesic tortuosity. The resulting 3D model was also used for finite element method (FEM) modelling to calculate the elastic modulus and ionic conductivity of the structure. The simulated results are compared with experimental values.

2 Materials

2.1 Carbon fibre electrodes

Carbon fibre is a material commonly used in lightweight applications. Carbon fibres are often used together with polymer matrix materials to form carbon fibre reinforced composites. This is mainly due to the high specific modulus and specific strength of carbon fibres. Common carbon fibres such as T800 and T1000 have a modulus of 294 GPa in the axial direction and a density of only 1.8 g/cm^3. This corresponds to a specific modulus of 163 GPa/(kg/m^3), which is six times higher than that of steel (27 GPa/(kg/m^3)).

The properties of carbon fibres are derived from their atomic structure. Carbon fibres are fibrous materials made up of more than 90 % of carbon atoms. The diameter is approximately 5 to 10 μm. Common structures of elemental carbon in nature are diamond and graphite. Their crystalline structures are plotted in Figure 3. In diamond, all carbon atoms are covalently bonded to form face-centred cubes. In graphite, carbon atoms are covalently bonded to form graphene, which is then van der Waals bonded and stacked on top of each other in the sequence of ABAB…. The graphite structure is thermodynamically stable, while the diamond structure is metastable. The specific structure of a carbonaceous material depends on the specific manufacturing process. In the case of carbon fibres, polymer precursors are first extruded into filaments. Currently, over 90 % of carbon fibre precursors are polyacrylonitrile (PAN). This is followed by a preheating phase in air (200 to 300 °C), This step is also generally known as the stabilisation process. This is then followed by the carbonisation stage, which is heating the fibres to 1000 to 1700 °C in an inert gas atmosphere. The high temperature causes the decompositions of the hydrogen, oxygen and nitrogen elements. After the heat treatment, carbon fibres often have a carbon content of 90 % or more [15]. Finally, a graphitisation process can also be added, i.e., heating to 2000 to 3000 °C in the inert gas atmosphere to obtain a higher carbon content and a more graphite-like crystal structure. It is important to note that to obtain a graphitic structure, the precursor must be able to form a semi-liquid state during the decomposition. Only in the semi-liquid state can the hexagon rings of carbon atoms be rearranged to form a parallel state to each other [16]. If there are too many cross-linked bonds in the organic precursor, then the semi-liquid state cannot be formed. Consequently, the crystalline structure of graphite cannot be formed either. The most common PAN precursor is the one with cross-linked bonds. Therefore, a pure graphitic crystalline structure cannot be formed in such carbon fibres, instead, a turbostartic graphitic structure is formed.

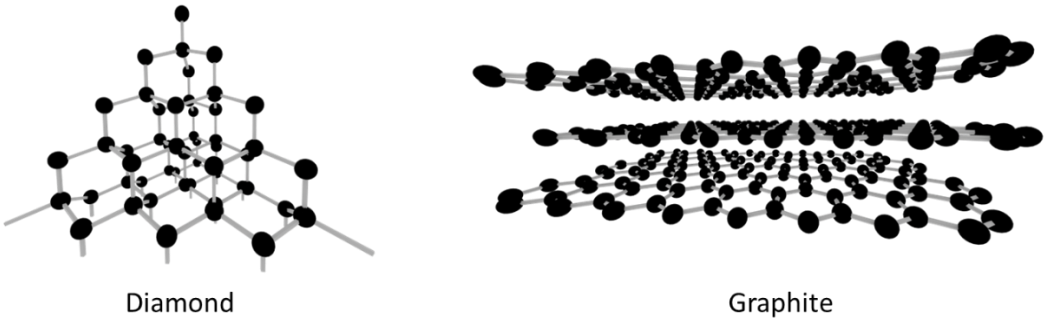

Figure 3. The allotropic structures of carbon.

In carbon fibres, the orientation of the grains is very anisotropic. The graphene planes are almost parallel in the axial direction. This results in carbon fibres that are covalently bonded in the axial direction and have an extremely high specific modulus, whereas in the radial direction the fibre is partially bonded by weak van der Waals bond and the transverse modulus is often only 10 to 20 % of that in the axial direction.

Graphite is an excellent electrode material because its large graphene interlayer spacing (3.35 Å) facilitates the repeated intercalation and deintercalation of lithium ions. Carbon fibres have a disordered layered structure like that of graphite, making their properties similar but different. Firstly, like graphite, carbon fibres can also be used as a hosting body for lithium ions. However, carbon fibres have small nano-sized grains, more defects and larger interlayer distances. As shown in Figure 4, the smaller the grain size, the higher the energy density of the carbon fibre for the thickness lower than 7 nm. These small grains carbon fibres tend to have an intermediate elastic modulus and are also known as IM carbon fibres. In contrast, carbon fibres with higher graphitisation and higher modulus have a lower energy density. For example, the M60J carbon fibre has an energy capacity around 100 mAh/g.

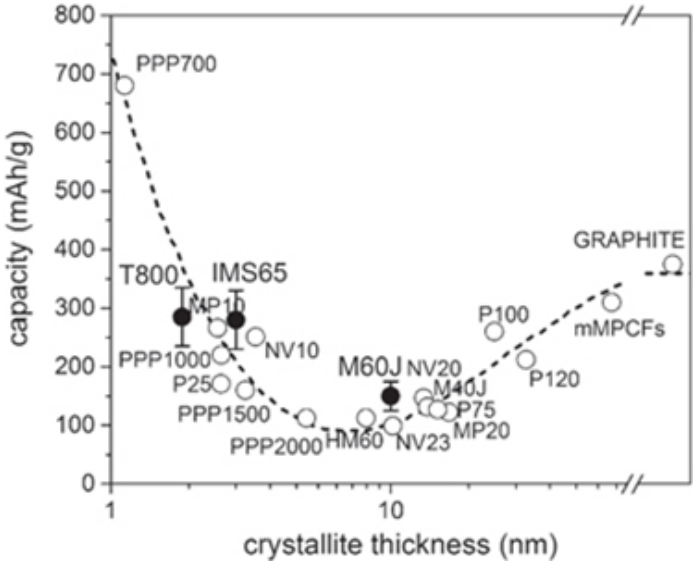

Figure 4. Energy density of carbon materials as a function of grain size [17,18,19].

In this thesis, the main carbon fibres discussed are IMS65, T800 and M60J. They are all PAN-based carbon fibres, with IMS65 and T800 being intermediate modulus carbon fibres and M60 being a high modulus carbon fibre. Their electrochemical properties have been well investigated and are listed in Table 1 [17,20].

Table 1. Basic parameters of different carbon fibres from literatures [17,20].

Carbon fibre	IMS65	T800	M60J
Interlayer spacing	3.49 Å	3.70 Å	3.47 Å
Crystal thickness	28 Å	18 Å	>100 Å
First charging capacity (mAh/g)	350	265	159
First discharging (mAh/g))	228	200	154
Normalized first cycle loss	36%	48%	16%
10^{th} cycle coulometric efficiency	99.54	99.93	99.47
Electric resistance (Ωcm $\times 10^{-3}$)	1.45	1.4	0.7

2.2 Structural battery electrolyte

SBE is a bi-continuous semi-solid polymer electrolyte composed of nano-pores filled with a liquid electrolyte. To achieve the multifunctionality, energy storage capacity and force-bearing capability of a structural battery, the SBE must be at least partly solid. Although the carbon fibre anode is the main contributor to the mechanical properties of the structural battery, the load transfer between carbon fibres must be achieved via a solid material. Although the liquid electrolyte has excellent electrochemical properties (ionic conductivity of 10^{-2} S cm^{-1} [21]), the inability of the liquid to transfer mechanical load makes the carbon fibres to crumble or twist under compressive or shear loads and they become useless as a structural component. In addition, a solid electrolyte is also safer compared to liquid electrolytes. In short, a solid electrolyte is a fundamental requirement for the realisation of a structural battery.

The most important properties of a solid-state electrolyte are its ionic conductivity and elastic modulus. Common solid-state electrolytes are solid inorganic electrolytes and solid polymer electrolytes. By nature, solid inorganic electrolytes should be ideal for structural batteries because they have both a high ionic conductivity (>10^{-4} S cm^{-1}) and a high elastic modulus (>1 GPa) [5]. However, solid-state inorganic electrolytes tend to be brittle and normally have poor interfacial conductivity, which makes them difficult to apply in structural batteries. On the other hand, solid polymer electrolytes are easier to synthesis, have high elasticity and good interfacial properties, making them more suitable for the manufacturing of the structural batteries. However, in solid polymer electrolytes, ions are transferred through polymer chains and therefore their ionic conductivity and elastic modulus tend to be negatively correlated [22]. To overcome this problem, Professor Mats Johansson and his research group designed a porous electrolyte material [23,24]. The porous structure is formed by polymerization induced phase separation (PIPS) [24]. The electrolyte is semi-solid and contains two phases, one liquid phase and one solid backbone phase. The solid phase is responsible for the mechanical integrity of the whole system and the liquid phase in the pores is responsible for the ionic conductivity. This electrolyte demonstrates good ionic conductivity and mechanical properties.

The SBEs used in Paper A and Paper E have this porous structure. Synthesis of the SBE is convenient (Figure 5). First the electrolyte including the organic solvent and the lithium salt are mixed in a glove box filled with argon gas. Then the monomer, electrolyte and heat curing

initiator are mixed of a certain ratio. The materials and ratios used in Paper A and Paper E are listed in Table 2.

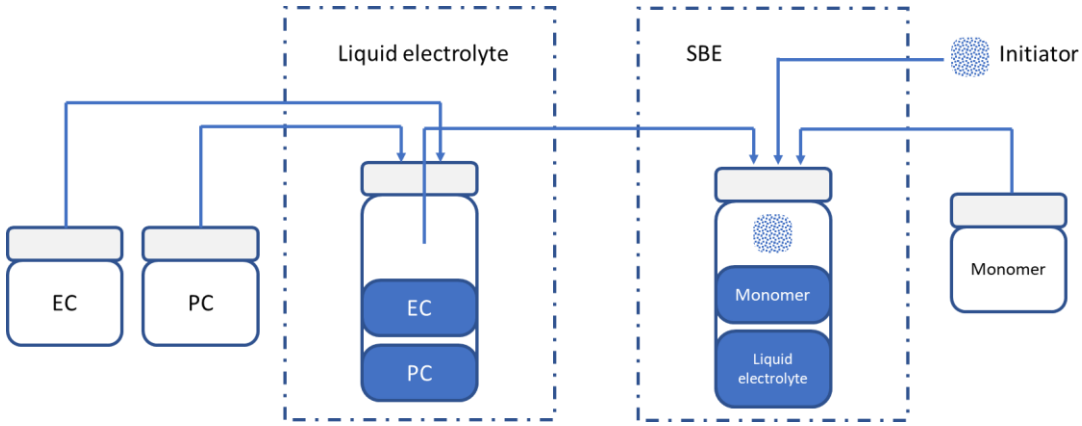

Figure 5: Synthetic route of SBE. EC: Ethylene carbonate, PC: Propylene carbonate.

Table 2. Specification of the SBE materials used in papers A and E.

	Paper A	Paper E
Monomer	Bisphenol A ethoxylate dimethacrylate	Bisphenol A ethoxylate dimethacrylate
Liquid solvent	EC 50wt% + PC 50wt%	EC 50wt% + PC 50wt%
Lithium salt	lithium trifluoromethanesulfonate (LiTf)	bis(trifluoromethanesulfonyl)imide (LiTFSI)
Lithium concentration	1 M	1M
Weight ratio of liquid electrolyte	50 wt%	45 wt%
Initiator	2,2′-azobis(2-methylpropionitrile)	2,2′-azobis(2-methylpropionitrile)
Initiator weight ratio to SBE	1%	1%

2.3 Structural Batteries

Structural batteries were first proposed by US Army Research Labs (ARL) [25,26]. They used a carbon fibre laminate as the anode, a stainless-steel foil coated with lithium iron phosphate (LFP) as the cathode and a glass fibre separator. However, the electrochemical performance of the cells could not be measured due to the poor insulation. Liu et al. [27] fabricated a structural battery with short carbon fibres reinforced cathode and a gel electrolyte. The structural battery has a high energy density (35 Wh/kg) but a low elastic modulus (3 GPa). It is important to note that here the carbon fibres are only used for reinforcement and not as an active electrode material. Due to the unavailability of suitable carbon fibres, they used coke particles as anode. Moyer et al. [28] made a multifunctional battery, using carbon fibres as both current collector and reinforcement material. They did not use the fibres as active material but coated them with graphite powder and LFP on the anode and cathode, respectively. By using a liquid electrolyte,

a high energy density was obtained (35 Wh/kg) but this resulted in a relatively low elastic modulus (2 GPa).

In Paper A, by using the recently developed SBE in combination with the T800 carbon fibre anode, a structural battery with a good compromise between electrochemical and mechanical properties was produced. The battery has a reasonable energy density (24 Wh/kg) at lower current and a relatively high elastic modulus of 25 GPa. As shown in Figure 6, the multifunctionality of the structural battery is better than previous batteries from the literature. This is because the mechanical and electrochemical properties of carbon fibres is being used simultaneously. The material and specific production steps for this structural battery can be found in Paper A.

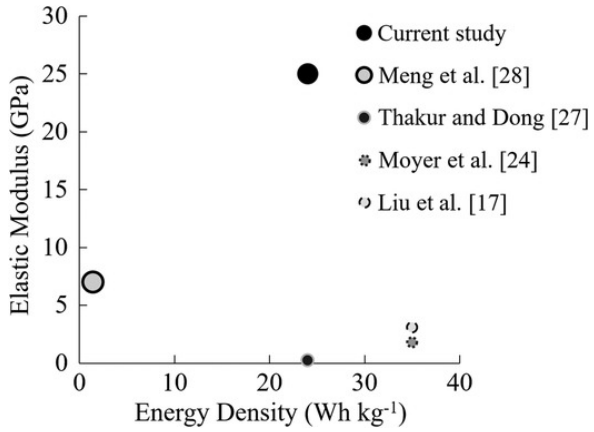

Figure 6. Energy density and elastic modulus of the structured battery (Paper A). The reference number is valid in Paper A.

3 Material characterisation methods

3.1 Scanning electron microscopy

Scanning electron microscopy (SEM) was used in all papers to locate, observe, and image the objects of study. Different equipment was used in different experiments, including the JEOL JSM-7800F Prime, LEO Ultra55, FEI Versa3D LoVac Dual Beam and Tescan GAIA3 (Tescan, Czech Republic). The SEM shoots focused electrons on the sample and analyses the resulting signal to obtain information about the surface of the sample. By scanning the surface of the sample, information is collected for each pixel, resulting in an image of the sample. The magnification of the SEM is therefore dependent on the minimum area scanned. The minimum area in turn depends on how well the electron beam is focused.

When the incident (primary) electrons bombard the sample surface, they interact with the sample in a volume of a certain depth. As shown in Figure 7, within the interaction volume different signals such as secondary electrons, backscattered electrons, characteristic X-rays etc. are generated [29]. The secondary electrons (SE) originate from the inelastic collisions of the incident electrons with the sample atoms. The inelastic collision causes the electrons of the sample atom to be excited by the incident electrons and leave the atom to produce secondary electrons. The number of secondary electrons is only related to the surface shape of the sample and is not affected by the atomic number of the sample. Backscattered electrons (BSE) are generated by the elastic collision of the incident electrons with the sample. The higher the atomic number of the sample, the higher the number of backscattered electrons generated. Backscattered electrons are primary electrons and therefore have a higher energy than secondary electrons. The characteristic X-ray is produced by the leap of the sample atoms. When an electron at a lower energy level is excited by an incident electron and leaves a vacancy, the electron at the higher energy level leaps to the lower energy level and releases an X-ray with an energy equal to the energy difference of the two energy levels.

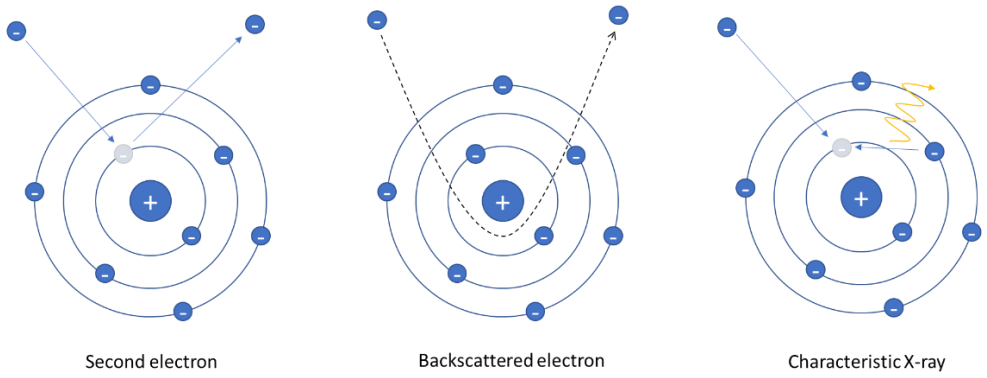

Figure 7. The mechanism of different signals in SEM.

In general for morphology characterisation secondary electrons are detected. This includes SEM images of the papers from A to D. However, the BSE is selected as the signal in paper E, due to a charging effect on the SBE surface. The charging effects tend to occur when the sample is non-conductive [30,31,32]. The charging effect is an imbalance of the electrical potential on the surface of the sample. This is often caused by more or less incident electrons than outgoing electrons. When the charging effect occurs, the image will have poor contrast and localised bright or dark areas. Secondary electrons are highly affected by the charging effect because they have low energy. The resulting image is blurred or distorted. To reduce the charging effect, non-conductive samples are often coated with a conductive layer. Normally, a 5 to 10 nm thick gold layer is applied depending on the sample. In paper E, the sample was coated with a gold layer about 20 nm thick and a platinum layer of 1 µm in thickness. However, as the observed surface is an in-situ cut surface, there is no conductive coating on the fresh cut surface. Even more, to obtain high resolution SEM images, electron immersion mode was used. In the electron immersion mode, a cage of electromagnetic fields covers the observation area so that the electrons cannot escape. This leads to a stronger charging effect. Therefore, BSE are chosen as the detection signal because the high energy of the BSEs makes them less susceptible to the charging effect.

3.2 FIB/SEM

The FIB/SEM technique was used in papers B and C to prepare smooth surfaces for indentation experiments. In paper E, FIB/SEM was used to obtain a series of slicing images for 3D reconstruction. The former ones used the FEI Versa3D LoVac Dual Beam and the latter one used the Tescan GAIA3 (Tescan, Czech Republic). FIB/SEM is a well-established technique for accurate milling / cutting of samples. It is the most used method for the preparation of transmission electron microscope samples, a thin slice of approximately 100 nm thickness [33,34,35]. FIB/SEM consists of an electron column and an ion column. They are placed at an angle so that there is a fixed position in both the centre of the field of viewports of the SEM and the FIB. The height of this position is called the eucentric height. Since the SEM has been introduced in the previous section, only the FIB is described here.

The basic components of the FIB are an ion source, a vacuum chamber, and a gas injection system (GIS). A common ion source is the liquid metal ion source (LIMS). It can provide ion beams with an accuracy of 10 nm [36]. In this thesis, Ga^+ ions were used. Ga^+ ions have the advantages of low volatility, low melting point and high atomic weight. The FIB can be used for imaging, milling and deposition as shown in Figure 8:

Imaging

High energy heavy ions can also excite the outer electrons of the sample, known as secondary electrons. The SEs can be collected by the detector to characterise the surface of the sample. However, imaging with FIB is risk to damage the sample [37]. Low acceleration energy and beam current should be used for this operation.

Milling

Milling is the most important function of the FIB. High velocity heavy ions are accelerated, focused inside an ion column, and then bombarded onto the surface of the sample. When the energy of the ions is higher than the bond energy in the sample, the atoms of the sample are removed by physical sputtering.

Deposition

Deposition requires GIS working in conjunction with FIB or SEM. Deposition is used to bond the sample, protect the sample surface, and reduce the curtain effect [37]. The GIS injects the precursor gas onto the surface of the sample. The gas decomposes under the action of ions and secondary electrons to produce non-volatile and volatile products. The non-volatile products are deposited on the surface of the sample. Common deposition materials are Pt, Si, W and C.

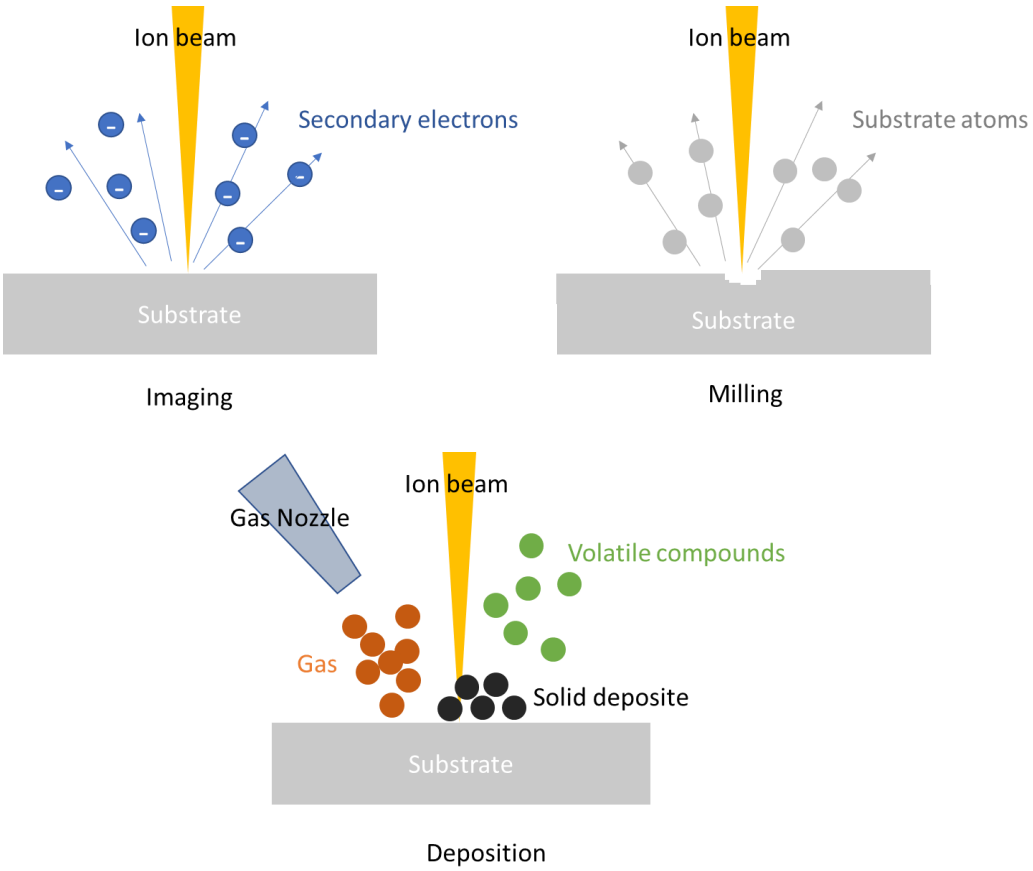

Figure 8. Schematic diagram of FIB operations: Imaging, Milling and Deposition.

3.2.1 Artifacts

3.2.1.2 Ion implantation and amorphization

When a sample is bombarded with high energy heavy ions, some of the ions penetrate the sample and embed in the sample. The depth of this embedment varies with the energy of the ions, the current of the ion beam and the sample material [38,39,40]. This artifact is referred to as ion implantation. As a result of the ion implantation, the sample loses its crystal structure and becomes amorphous. When 30 kV Ga^+ ions are used to mill silicon sample, the depth of the ion implantation can be up to 21 nm [38]. Although carbon fibres should be less affected compared to silicon, since the C-C covalent bond is stronger than that of Si, the exact implantation depth is unknown in carbon fibres. In papers B and C, the cut/milled surfaces are to be used for mechanical experiments. Once the crystal structure has changed due to the FIB cut, the mechanical properties of the material will also change. To ensure that the correct structure is obtained for mechanical experiments, ion implantation and amorphization defects must be cleaned sufficiently. The most effective and quickest way to clean the defected surface

is to use a low energy ion beam [41]. Giannuzzi et al. found that such defected layer could be reduced to 2 nm thick by using a low energy 5 KeV Ga^+ cleaning step [38]. It is expected that this method is sufficient to clean up defects on carbon fibre surfaces since as mentioned that the C-C bond is stronger than that in silicon. This is also confirmed in paper B.

3.1.2.2 Curtain effect

The curtain effect refers to the vertical streaks that appear on the cut surface of the FIB sample [37,42,43,44,45,46,47]. This artifact is caused by the fact that the milling speed of the FIB varies at different locations. In papers B and C, the artifact is not apparent. However, in paper E it is conspicuous since the object of the study, SBE, is a porous structure. In the non-porous region, the milling speed of the FIB is limited, while at the pores the milling speed can be seen as infinite. This results in a curtain effect that is difficult to avoid when using FIB to mill the SBE. The solution to this problem often must rely on later data or image processing [48,49,50]. The detailed method will be described in the data analysis section, or can be found in paper E.

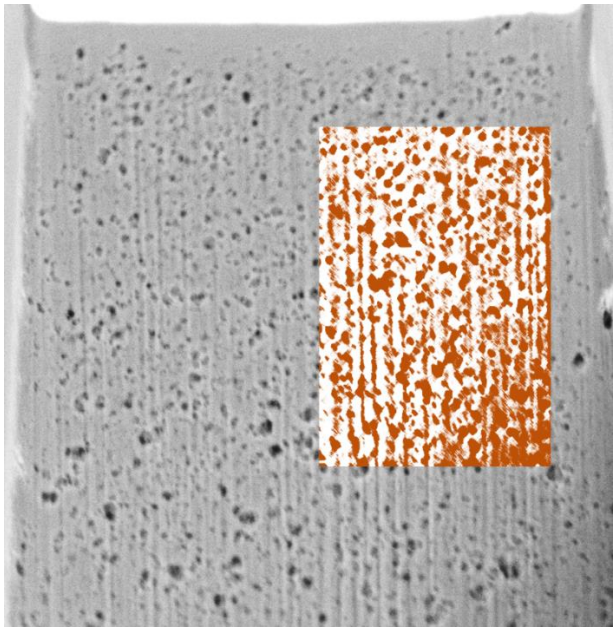

Figure 9. Examples of curtaining effects in a SEM image of FIB milled surface of a SBE. A local area (Orange) is adjusted to show the curtaining effect.

3.2.2 Workflow

In papers B and C, smooth, flat surfaces are milled on the single carbon fibres. There are two types of milled surface: parallel to the carbon fibre axis and perpendicular to the carbon fibre axis. The need for two surfaces is due to the derivation of the elastic contact model of orthotropic material later on. To fabricate the two different milled surfaces, two different workflows were used as shown in Figure 9. The specific preparation procedures can be found in papers B and C. Only the important steps are mentioned here. Samples parallel to the axial direction of the carbon fibre are easier to fabricate. The carbon fibre is placed on a flat silicon wafer and the sample stage is adjusted so that the ion beam is parallel to the surface of the silicon wafer. This can be achieved by looking directly on the carbon fibre through the FIB viewport. The surface perpendicular to the fibre axis is more difficult to fabricate. The difficulty is due to the requirement that the milled surface must face upwards to allow subsequent mechanical experiments. To ensure that the ion beam is perpendicular to the carbon fibre during

cutting, as shown in Figure 9, the carbon fibre must first be aligned with the ion beam, then the sample stage is rotated 180° horizontally and tilted by an angle of 14-α, where α is the titling angle of the sample stage in the first step. Note that the 14-α angle is derived from the angle of 52° between the ion column and the electron column. Pt deposition is applied to fix the cut short carbon fibres onto the Omniprobe and eventually onto the new sample stage. The limitation of the maximum tilting angle in the FIB/SEM makes it necessary to replace the sample stages during the process.

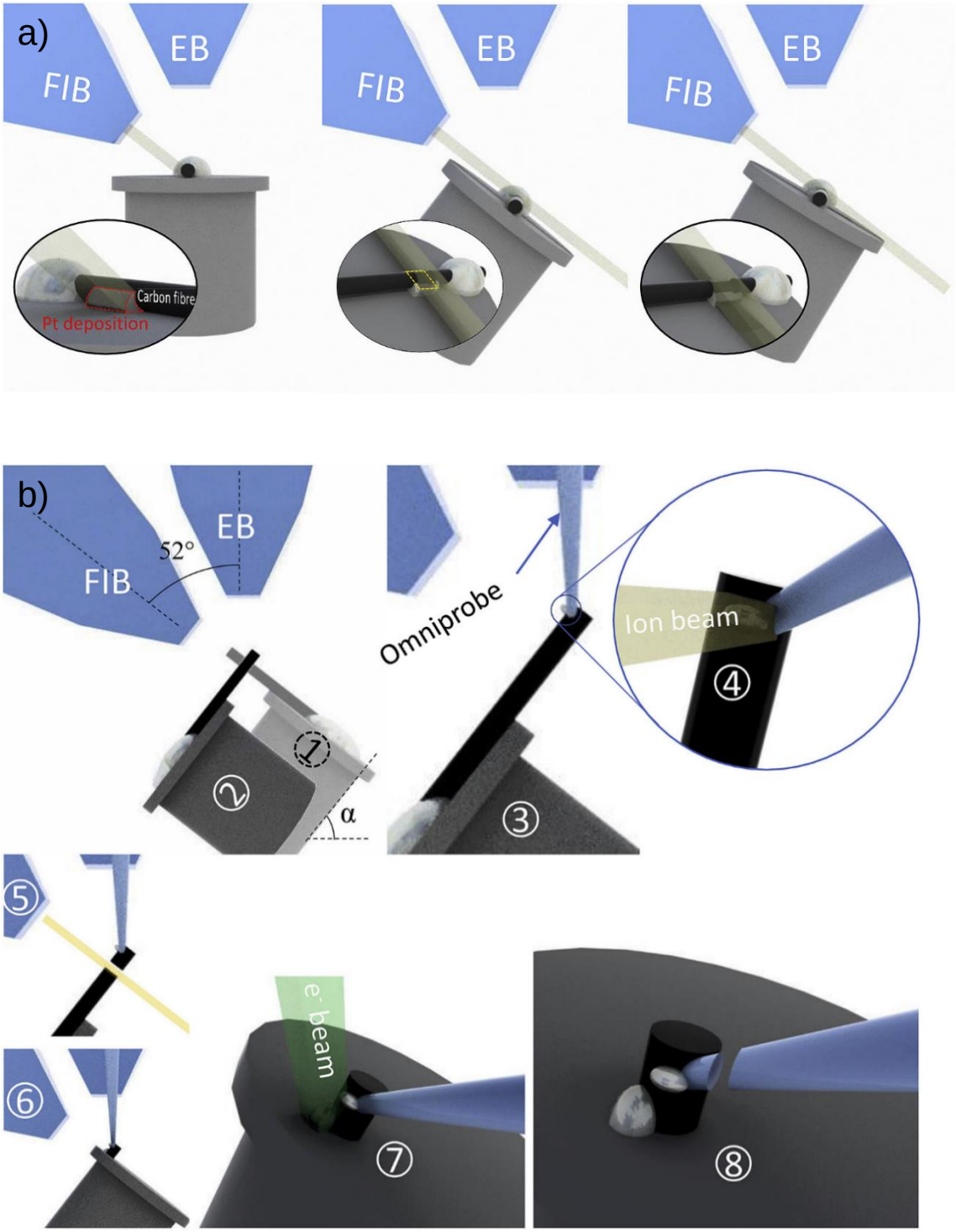

Figure 9. Schematic of the workflow for milling flat surfaces on carbon fibre. a) The flat surface is parallel to the fibre axis. b) The flat surface is perpendicular to the fibre axis.

In paper E, FIB/SEM was used for the 3D reconstruction of an SBE. To obtain continuous slicing images of the sample, a T-shape was cut out at the edge of the sample as shown in Figure 10. A reference pattern was then milled on the T-shape. This reference pattern was used as a location reference in subsequent cuts and imaging to counteract location errors arising from sample drift. The FIB milling and SEM imaging were controlled by a computer programme, starting at the end of the T-shape and gradually inside by every 20 nm in each step. To obtain sufficient resolution to observe the nanoscale pores in the SBE, electron immersion mode was used. As explained in section 3.2.1, the non-conductive sample plus the use of the electron immersion mode results in a strong electron accumulation on the sample surface and causes a large drift of the sample. Typically, after 30 to 40 cuts, the marker pattern would leave the marker view window and result in an incorrect calibration. In paper E, a set of stable results with 60 stable milled surface images is used for subsequent 3D reconstructions.

The FIB parameters used in papers B, C and E are summarised in Table 3.

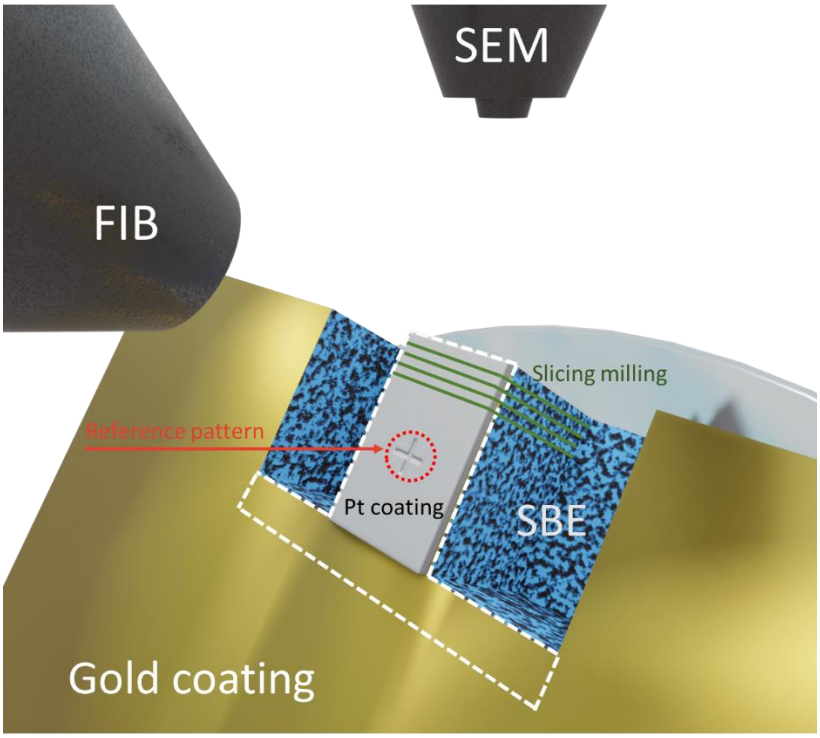

Figure 10. Schematic of the setup for milled surface imaging from paper E.

Table 3. The FIB parameters used in papers B, C and E.

	Papers B and C	Paper E
Ion beam voltage	30 kV	30 kV
SEM detector	In lens SE	Mid-Angle BSE
SEM beam voltage	15 kV	2kV
Final FIB milling current	0.5 nA	0.25 nA
Cleaning current	0.08 nA	-
Cleaning Voltage	2kV	-
Coating material	Pt	Pt

3.3 Atomic force microscope

An atomic force microscope (AFM) was used to do indentation experiments in papers B and C. A MultiModeIII with Picoforce extension (Veeco Instrument, Santa Barbara, CA, USA) was employed. Since its invention in 1986 [51], the AFM has been used extensively in the fields of electronics, polymers, and biomaterials [52]. AFM is particularly important in the biological field [53,54,55,56] because it can be used in air and even in liquids [57]. A schematic representation of an AFM is shown in Figure 11a. The basic components of an AFM are a micro-cantilever, a probe, a piezoelectric scanning system and a micro-cantilever bending sensing device. AFM obtains information about the sample surface by precisely sensing the intermolecular forces between the probe and the sample (nanoNewton or picoNewton). To precisely sense the intermolecular forces, a laser beam shoots onto the micro-cantilever and reflects back to the detector. Under the influence of intermolecular forces, the bending of the micro-cantilever causes a change in the reflected optical path and ultimately in the position of the laser spot on the detector. The slight change in reflection angle causes a measurable change in position after passing a long optical path. Through this amplification effect, even pico-Newton force can be measured. This molecular force is shown in Figure 11b. When the probe is in close proximity to the sample, the probe first feels an attractive force. Upon continued approach, the attractive force eventually becomes repulsive. In the different operation modes Figure 11c, different types of force are detected.

- Contact mode: Direct contact between the probe and sample; It is featured by high resolution but also high risk of sample damage. Repulsive force is measured.

- Non-contact mode: Probe at a fixed distance from the sample; It is featured by low resolution with high sample safety; Attractive force is measured.

- Tapping mode: The probe strikes the sample surface rapidly at its resonant frequency. It is featured by both high resolution and high sample safety. Repulsive force is measured.

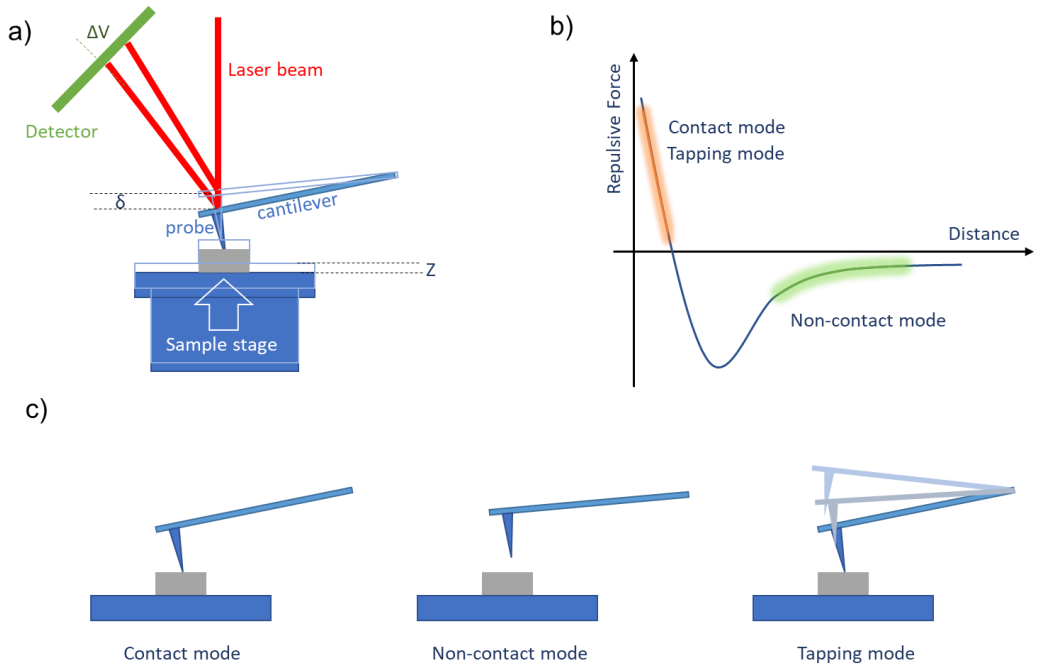

Figure 11. a) Schematic diagram of an AFM. b) Intermolecular force and c) Schematic diagram of the different operation modes of the AFM.

The different modes of operation are primarily intended to protect the sample. During translation movement of the probe, the shear stress in front of the probe and the sample is often the main cause of damage to the sample or probe. In non-contact mode, the shear stress is zero. In tapping mode, there is only normal stress and no shear stress. Therefore, the tapping mode is considered as safe as non-contact mode.

Combined with the ability of the AFM to measure forces, the AFM has also been widely used in nanoindentation experiments [58,59,60,61]. In papers B and C, an AFM is used to perform nanoindentation experiments. Diamond probes with a tip radius of 30 nm were used to perform approximately 30 indentation experiments on each sample. The maximum depth of each indentation was limited to 10 nm to avoid any plastic deformation. As the AFM was only equipped with an optical microscope from top view and the micro-cantilever hide the probe position, it was not possible to position the probe directly onto the cut surface. To find the cut surface for the nanoindentation experiments, a linear scan near the cut surface was first performed using ramping mode. The upper limit of the contact force was set very low to avoid damaging the sample or the probe. The centre of the section is determined by looking at the height information of each ramp point. In the nanoindentation experiments, the indentation force and indentation displacement are recorded. They are derived from Eqs. 1 and 2 by combining the actual recorded sample stage height Z, the deflection voltage ΔV with the spring constant of the probe, k, the deflection of the micro-cantilever, δ, and the sensitivity of the detector, ε.

$$D = Z - \delta = Z - \Delta V \times \varepsilon \tag{1}$$

$$F = k \times \delta = k \times \Delta V \times \varepsilon \tag{2}$$

Since the spring constant k is different for different probes and the sensitivity of the detector, ε, is uncertain, the experimental results must be calibrated. The conventional method of calibration is to perform an extra indentation experiment on a standard sample and to treat the standard sample as having an infinite modulus. The resulting indentation curve is used to calibrate the indentation curve of the sample. This method is generally suitable for samples with low modulus, such as biological materials. However, the carbon fibre is also a high modulus material and therefore the assumption that the modulus of the standard sample is considered to be infinite is incorrect and introduces large errors. In paper C, a new analytical method is proposed to accurately calibrate the experimental results by combining the indentation curves of two different standard samples. This analytical method is introduced in the chapter of data analysis.

3.4 Nanoindentation

Nanoindentation is a well-established technique for mechanical tests [62]. Initially nanoindentation was used to measure the hardness of materials, but it was later discovered that information such as the elastic modulus was also included in the indentation curve [63]. In contrast to AFM, nanoindentation directly measures the force and displacement using piezoelectric elements (Figure 12a). The general force accuracy is nano-Newton, and the displacement accuracy is 0.1 nm [62].

In papers B and C, nanoindentation test is performed by Brucker's Hysitron TI 980 TriboIndenter (Figure 12c). The tip radius is around 150 nm, and the indentation depth is around 100 nm. 3D morphology of the probe is measured by scanning probe microscopy (SPM). This data provides the actual contact area between the probe and the sample. In paper D, compression test was implemented by a hand-size indenter from Alemnis AG, which is capable to operate

in a SEM. A plat punch probe is used to compress a lying carbon fibre (Figure 12c). The tip is made of tungsten carbide (ALM/FLT060/D100/WC/UHT (60° cone angle)) from Synton-MDP AG. The diameter of the flat punch is measured as 107 µm by SEM.

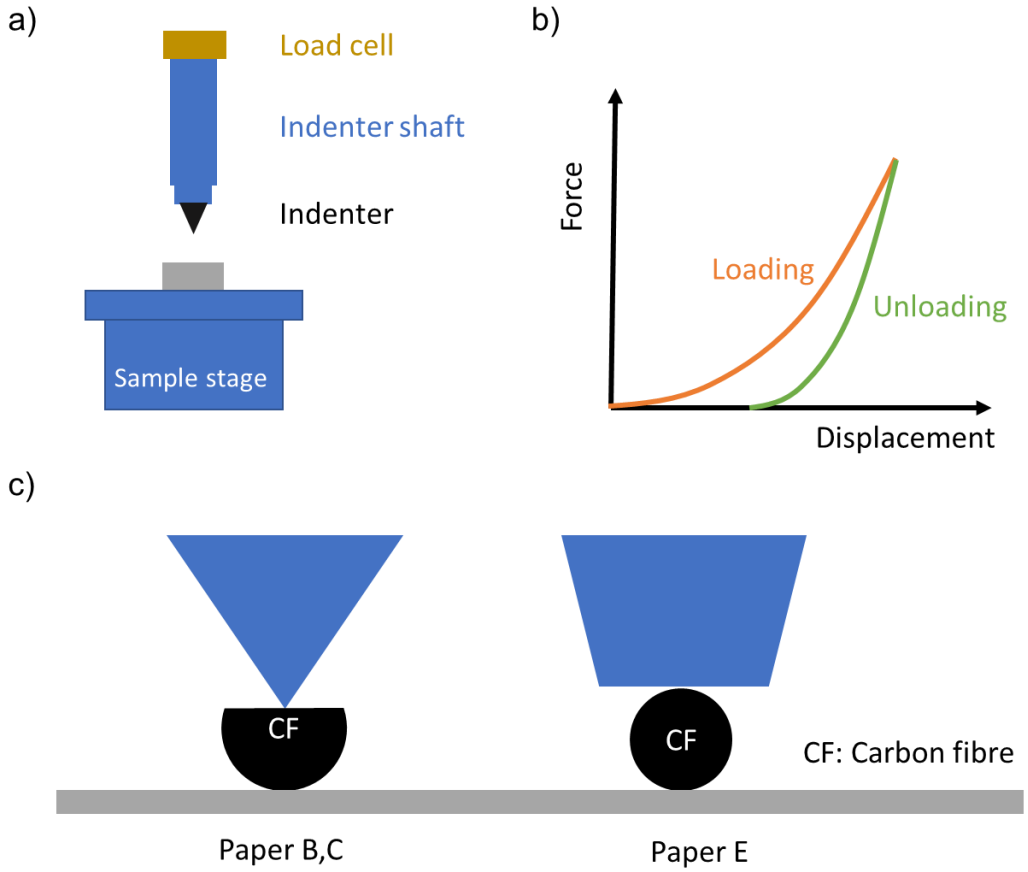

Figure 12. a) Schematic diagram of the nanoindentation instrument. b) Typical indentation force-displacement curve. c) Schematic diagrams of the nanoindentation experiments in papers B, C and the compression experiments in paper D.

4 Data analysis methods

This chapter introduces data processing and analysis methods. This includes data obtained from nanoindentation experiments, compression experiments on carbon fibre anode and 3D model reconstruction of the SBE. The force-displacement curves obtained in the different mechanical experiments need to be transformed into the elastic modulus of the material according to the corresponding mechanical model and the geometry. It is important to note that nanoindentation experiments are performed by both nanoindentation and AFM. The AFM has a higher force accuracy; however, the force is not directly measured. A special, self-developed calibration method is required. In addition to the indentation model, an orthotropic elastic contact model is also required. This is because the moduli derived by the conventional indentation model represent the response of the whole material. Whereas, due to the strong anisotropy of carbon fibres, the modulus in a particular direction can be higher or lower than the overall effective properties of the material. Finally, in the case of 3D reconstruction of SBE, the obtained slice images need to be post-processed, segmented and reconstructed in computer.

4.1 Pharr-Oliver model

The Pharr-Oliver contact model is the most traditional model used to analyse nanoindentation curves [64]. A typical nanoindentation curve is shown in Figure 12b. The loading curve is considered to include both elastic and plastic deformation and therefore this part of the curve is not used to derive the elastic modulus. In the unloading curve, on the other hand, the material releases its stored elastic energy via pure elastic deformation. The unloading curve follows a power-law,

$$P = \alpha\left(h - h_f\right)^m \tag{3}$$

where α and m are fitting parameters, P is the force, h is the indentation displacement and h_f is the indentation displacement after unloading. The effective indentation modulus E^* of the system can be obtained from the initial part of the unloading curve

$$E^* = \frac{S\sqrt{\pi}}{2\beta\sqrt{A_c}}, \tag{4}$$

where S is the slope of the unloading curve, β is the geometrical parameter, and A_c is the contact surface area between the indenter prob and the sample. In the experiments, the contact area is obtained from the 3D topological information from SPM scanning. Note that the indentation modulus of the system also includes the compliance of the system. To obtain the elastic modulus of the sample material, the compliance of the system needs to be excluded

$$\frac{1}{E^*} = \frac{1-\upsilon_i^2}{E_i} + \frac{1-\upsilon^2}{E} \tag{5}$$

where υ and E are the Poisson's ratio and Young's modulus of the sample and υ_i and E_i are the Poisson's ratio and Young's modulus of the indentation probe material.

4.2 Hertzian contact

The Hertzian contact model describes a sphere in purely elastic contact with a flat surface [65]. Unlike Pharr-Oliver, loading curves are used. Although the loading curve may contain plastic deformations, by limiting the maximum load and use only the initial part of the curve, purely elastic indentation curve can still be ensured. In the Hertzian contact model, the force F is a function of the indentation depth D, as

$$F = \frac{4}{3}E^*\sqrt{RD^3} \tag{6}$$

where R is the radius of the sphere. This equation can also be rewritten so that D is a function of force F,

$$D = F^{\frac{2}{3}}\left(\frac{4\sqrt{R}}{3}E^*\right)^{-\frac{2}{3}} \tag{7}$$

Here E^* can be derived from the slope of the curve $D\ vs.\ F^{2/3}$. The equation will be used in the AFM calibration section.

4.3 Ward model

The Ward model describes the force vs. the diameter variation of an anisotropic fibre under lateral compression [66,67,68]. The Ward model is used in the unloading curves of the compression experiments to derive the transverse modulus of carbon fibres in paper D. The Ward model has been successfully used in other works to determine the transverse modulus of carbon fibres [69,70]. In the Ward model, the displacement of the indenter U is a function of the compression load F as

$$U = \frac{4F}{\pi}\left(\frac{1}{E_t} - \frac{\upsilon_{lt}^2}{E_l}\right)\left(0.19 + sinh^{-1}\frac{R}{b}\right) \tag{8}$$

$$b^2 = \frac{4FR}{\pi}\left(\frac{1}{E_t} - \frac{\upsilon_{lt}^2}{E_l}\right) \tag{9}$$

Where E_t is the transverse modulus of the carbon fibre, E_l is the longitudinal modulus of the carbon fibre, υ_{lt} is the Poisson's ratio and R is the radius of the carbon fibre.

Normally it is valid to assume that $\upsilon_{lt}^2/E_l \ll 1/E_t$, and Eqs. 8 and 9 can be simplified as

$$U = \frac{4F}{\pi E_t}\left(0.19 + sinh^{-1}\frac{R}{b}\right) \tag{10}$$

$$b^2 = \frac{4FR}{\pi E_t} \tag{11}$$

4.4 AFM calibration

As described in the previous chapter, to obtain the force and displacement in the indentation experiment in AFM, the detector sensitivity and spring constant of the microcantilever are required. However, both the detector sensitivity and the micro-cantilever spring constant are unknown quantities. When using only one standard sample to calibrate, it is necessary to first assume that the probe cannot be pressed into the standard sample to derive the deformation of the probe tip. The assumption that the standard sample cannot be pressed does not apply in this work because the high modulus of the carbon fibre is comparable to that of the standard sample. An incorrect calibration causes an incorrect force vs. displacement curve. The slope calculated using Eq. 7 can also introduce errors. Note that when the same voltage range is used for both the standard sample and the carbon fibre, the error caused by the incorrect calibration is a constant value (Eqs. 1 and 2). That means the error in the slope calculation in Eq. 7 is also a constant value for a fixed voltage range, with m representing the slope derived from the incorrect calibration and m^o representing the true slope. Then for both samples and standards there is the formula

$$m_x = {m_x}^o + \Delta m_x \tag{12}$$

where the notation x represents the sample being tested, which can be either an experimental sample or a standard sample. When two different standard materials are tested, the following equations can be derived

$$m_{sample} - m_{standard\_1} = {m_{sample}}^o - {m_{standard\_1}}^o \tag{13}$$

$$m_{standard\_1} - m_{standard\_2} = {m_{standard\_1}}^o - {m_{standard\_2}}^o \tag{14}$$

Define a value C as Eq. 13 divided by Eq. 14,

$$C = \frac{m_{sample} - m_{standard\_1}}{m_{standard\_1} - m_{standard\_2}} = \frac{{m_{sample}}^o - {m_{standard\_1}}^o}{{m_{standard\_1}}^o - {m_{standard\_2}}^o} \tag{15}$$

It can be seen that the constant value C can be obtained from three different slopes with experimental errors. Note that C can still accurately describe the relationship between the three different true slopes. Since m^o is the true slope, it follows from Eq. 7 that

$${m_x}^o = \left(\frac{4\sqrt{R}}{3}{E_x}^*\right)^{-\frac{2}{3}} = A{E_x}^{*-\frac{2}{3}} \tag{16}$$

where A is a constant value when the same indenter probe is used. Now combining Eqs. 15 and 16,

$$C = \frac{{E^*_{sample}}^{-\frac{2}{3}} - {E^*_{standard\_1}}^{-\frac{2}{3}}}{{E^*_{standard\_1}}^{-\frac{2}{3}} - {E^*_{standard\_2}}^{-\frac{2}{3}}} \tag{17}$$

$$E^*_{sample} = \left(\frac{{E^*_{standard\_1}}^{-\frac{2}{3}} + (C-1){E^*_{standard\_2}}^{-\frac{2}{3}}}{C}\right)^{-\frac{3}{2}} \tag{18}$$

It is also important to note that E^* in the equation are still the indentation moduli. They can be derived from the Young's modulus and Poisson's ratio for the material and the material of the indentation probe according to Eq. 5.

In summary, by comparing the indentation results of the sample with two different standard samples, the correct indentation modulus can be found. The developed method solves the difficulty and makes AFM suitable for testing high modulus samples.

4.5 Swanson's orthotropic contact model

For isotropic materials, the Young's modulus of a material can be calculated by Eq. 5 once the indentation modulus of the material has been obtained. This is because for isotropic materials, only two independent elastic constants exist. In practice, the deformation of the material in an indentation experiment is complex. It involves compression deformation in the direction of the indentation, tensile deformation in the direction perpendicular to the indentation and shear deformation. In short, the effective elastic modulus of the indentation test involves all elastic constants. For an isotropic with only two independent elastic constants, the Young's modulus can be calculated with an assumption of Poisson's ratio. However, carbon fibres are orthotropic materials, and as such possess five independent elastic constants which can be represented as

$$E^* = f(E_l, E_t, G_{lt}, \upsilon_{lt}, \upsilon_{tt}) \tag{19}$$

where E is Young's modulus, G is shear modulus, and υ is Poisson's ratio. The notations l and t represent the longitudinal and transverse directions, respectively. The Poisson's ratios are difficult to measure. Here we assumed their values. In paper C, the influence of the choice of Poisson's ratios on the resulting transverse and shear moduli was shown to be very small. Furthermore, the longitudinal Young's modulus of carbon fibres can be measured relatively accurately in uniaxial tensile tests. Here we obtain the data directly from the manufacturer of the carbon fibres. Thus, now only two unknown constants E_t and G_{lt} influence E^* in Eq. 19. That means that when an E^* is determined, the relationship between E_t and G_{lt} has also been determined. In paper C, E^* is measured in two different directions. This results in two functions for the relation between the two unknown quantities. As long as the two functions are independent, both unknown quantities can be determined. In practice, however, the Eq. 19 cannot be written in an exact analysed expression. This is mainly because the shape of the contact area of the indentation is elliptical, while the eccentricity of the ellipse is unknown.

Swanson proposed a model to calculate the correct indentation modulus that is iteratively approximated when the elastic properties of the orthotropic material are known [71]. At the start of the calculation, a set of elastic properties are defined, and the contact area is assumed to be circular. The model will then calculate the indentation modulus and the shape of the contact area. The newly calculated contact shape is compared with the shape in the previous calculation loop. If there is a discrepancy, the newly calculated contact shape is taken as a known quantity and a new indentation modulus and contact area is calculated. The loop, illustrated in Figure 13, will run until the difference between the new contact area and pervious one is sufficiently small. Converged result is often obtained after 4 cycles.

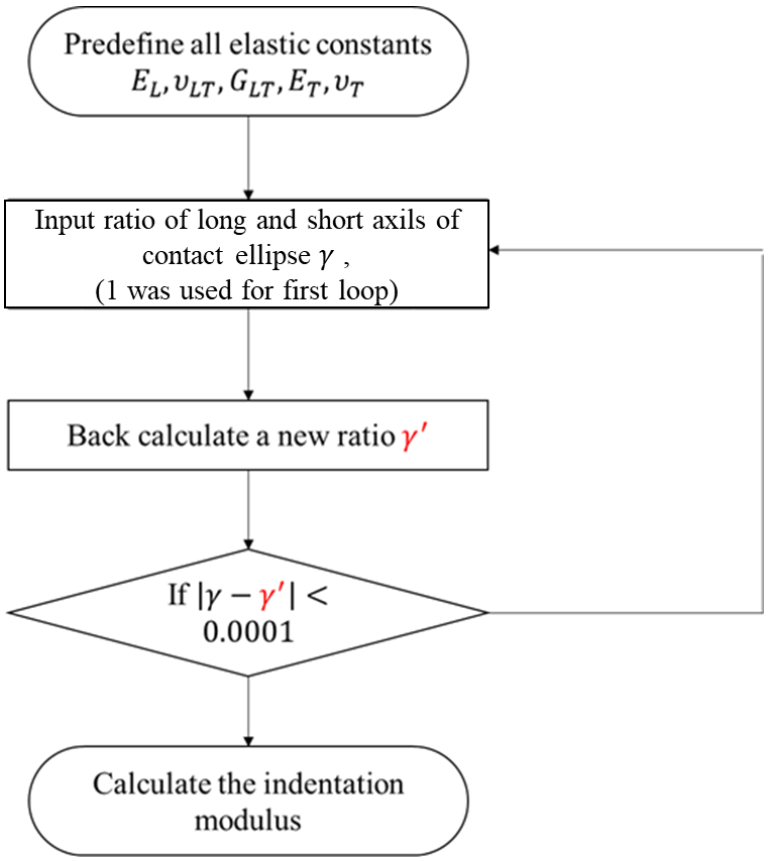

Figure 13. Work flow of the Swanson model [72].

4.6 3D reconstruction

3D reconstruction refers to the conversion of successive milled surface images into a 3D voxel model. In paper E, 60 milled surface images of the SBE were obtained by FIB/SEM. Each image was spaced at 20 nm. The brightness of the pixel was analysed to determine the phases, either polymer skeleton or pore. The milled surface images were arranged in 3D space at the correct spacing as shown in Figure 14c. The porous phase is removed. The remaining pixels are then stretched out of the image plane to voxels and form a 3D voxel model. However, the milled surface images obtained from FIB/SEM normally have defects, such as the curtain effect from the FIB milling as introduced in previous chapter, and the drift in the position of the images. These defects had to be addressed before the 3D reconstruction, otherwise an inaccurate model would be obtained.

4.6.1 Removal of the curtain effect

The curtain defects produced on the SBE milled surface are very visible (Figure 9 and 14a). In the absence of processing, these vertical lines would be treated as vertical polymer skeletons or pores in the following segmentation step. To remove these defects, few image processing steps are applied on these images. Because these vertical streaks are very similar to the strip noise in remote sensing, different de-striping methods developed over the last decades can be applied. These include the Fourier based filtering methods [73, 74] and wavelet analysis methods [75,76]. In paper E, the wavelet analysis method is applied. A general simple filtering process is to first transform the image from the spatial domain to the frequency domain using the Fourier

transform. In the frequency domain, features at specific frequencies are filtered out as required. The image is then transformed from the frequency domain into a normal image in the spatial domain using the Fourier transform. The Fourier transform transforms a function into a sum of a set of sine and cosine functions, while the wavelet transforms expand the function into a sum of a family of wavelet functions [75]:

$$WTf_{a,b} = \frac{1}{\sqrt{a}} \int f(x)\psi(\frac{x-b}{a})dx \tag{20}$$

Fourier transformation tends to lose information in the presence of high-frequency features within an image, whereas wavelet analysis preserves local information better. As shown in Figure 14b, the vertical stripes caused by the curtain effect are well removed.

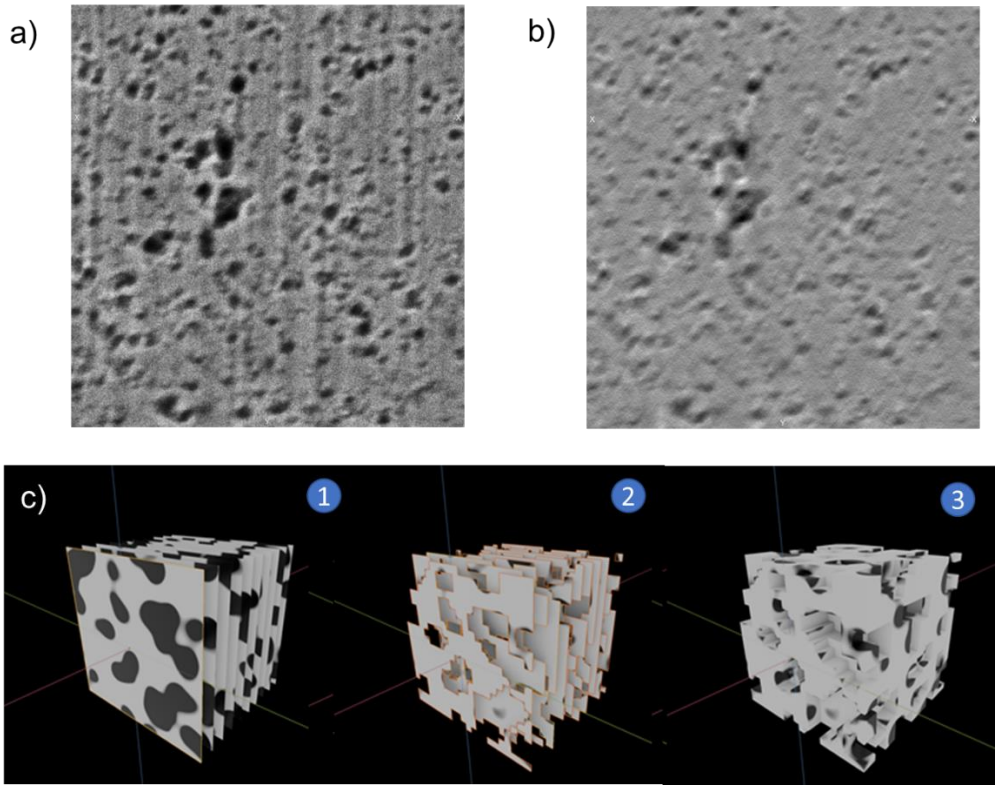

Figure 14. Schematic of image processing for 3D reconstruction from paper E. a) The image obtained from FIB/SEM and b) after destriping. c) Schematic illustration of the 3D reconstruction: 1) Segmented image stack. 2) Remove pore pixel, 3) Stretch the pixel to voxel.

4.6.2 Registration

In the FIB/SEM experiment, the sample drifted under the charging effect. Although the calibration was done by marking the pattern, the final image sequence still had positional deviations. In order to eliminate this deviation, the images were realigned by the sum of squared difference (SSD) method.

$$SSD = \int \int (image1 - image2)^2 \tag{21}$$

SSD calculates the sum of the squares of the differences of the grey values of the pixels in the same position. By re-aligning the image, the SSD value is minimised.

4.6.3 Segmentation

The polymer skeleton and pore phases in the SBE are segmented by a threshold method. By defining a greyscale value, a pixel is considered to represent the polymer when its greyscale is higher than the defined greyscale value. For a lower greyscale the pixel is considered to belong to a pore. As a result, higher threshold would result in a structure with lower porosity. The true porosity can be obtained by a simple calculation of the liquid phase content as 37.2%. The threshold value is adjusted to achieve the correct porosity.

5 Results and discussion

Paper A focuses on a structural battery and has been reported in sufficient detail in the Materials chapter. This chapter will focus on the characterisation results of the structural battery constituents. This includes the carbon fibre anode, the lithiated carbon fibre and the SBE. Detailed information can be found in papers B-E. The motivation and major results of each work are presented here.

5.1 Nanoindentation experiments with carbon fibres

The mechanical properties of the carbon fibre anode, as a major contributor to the multifunctionality of a structural battery, will be directly related to the mechanical properties of the structural battery. The mechanical properties of carbon fibres in the axial direction can be measured by a uniaxial tensile test. However, the transverse and shear moduli of the carbon fibre are challenging to measure due to the small size and high anisotropy of the carbon fibres. To measure the transverse modulus of carbon fibres, researchers have tried compression experiments, ultrasonic scattering and nanoindentation experiments [77,78,79,80,81,82]. In previous indentation experiments, indented surfaces were often prepared by mechanical cutting and polishing. This process can lead to amorphization of the sample surface. Besides, carbon fibres were treated as isotropic materials to calculate the transverse modulus even though the strong anisotropy of carbon fibres is well known. In fact, in an indentation experiment, the deformation produced by the sharp probe includes both compression and shear. Therefore, the indentation modulus contains information on not only the compression modulus but also the shear modulus. To extract the full information from an indentation modulus, Csanásdi et al. analysed the indentation modulus by means of a simplified formula [83] and derived five elastic constants of a carbon fibre [82]. It is important to note that the simplified equation assumes the contact area between the probe and the carbon fibre to be a circle. However, due to the anisotropy of the carbon fibre, this contact area should be an ellipse. To improve the experimental accuracy as well as the analytical model accuracy, the papers B and C used both AFM and nanoindentation to perform the indentation experiments on FIB fabricated carbon fibre samples and the results were analysed with an orthotropic contact model. This work not only succeeded in deriving the transverse and shear moduli of the carbon fibres, but also observed elastic hysteresis phenomenon of the carbon fibres under the nano-indenter. Unfortunately, this phenomenon is still ignored even in a recent work [84] even though the indentation curve obviously shows a hysteresis phenomenon.

5.1.1 Cleaning of the sample surface

As FIB cutting may cause Ga^+ ions implantation and amorphization of the turbostratic graphitic structure, low energy Ga^+ ions are used to clean the FIB milled flat surfaces. However, the effect of this cleaning cannot be directly observed, especially since the surface defects may only be a few nanometres thick. To assess and verify the experimental method of the surface fabrication, a set of experiments was designed in paper B (Figure 15): indentation experiments on an **uncleaned surface** to a depth less than 10 nm using AFM; indentation experiments on a **cleaned surface** to a depth of about 100 nm using a nanoindentation and to a depth less than 10 nm using AFM.

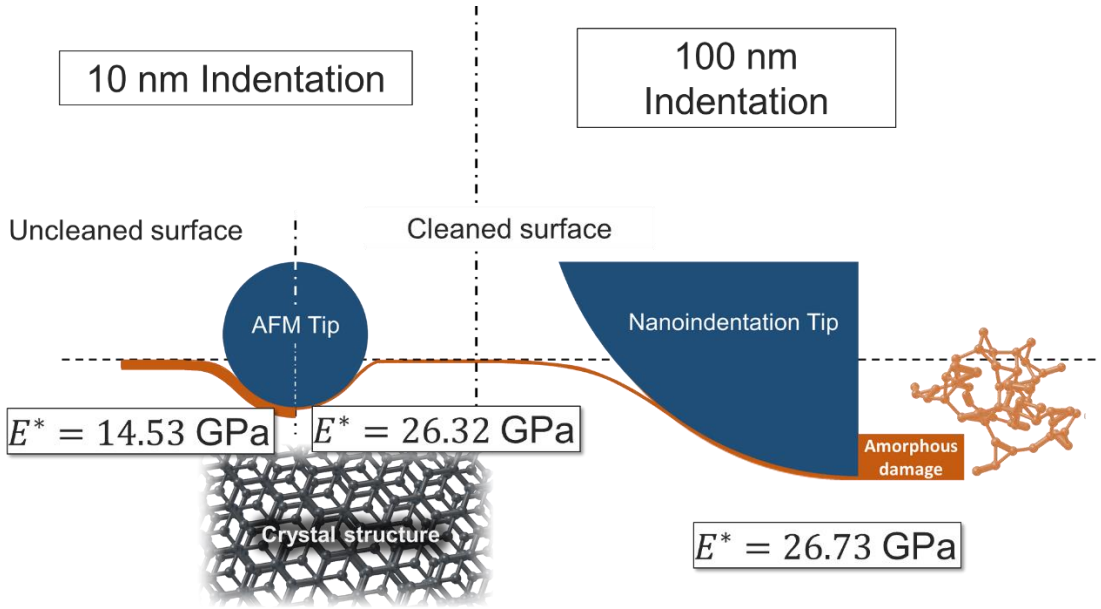

Figure 15. Schematic illustration of the experiments in paper B.

On the uncleaned surface, the AFM obtained an indentation modulus of 14.53 GPa, compared to the significantly higher indentation modulus of 26.73 GPa obtained by the nanoindentation on the cleaned surface. Although the mechanical models for the calculation are different (Hertz model for AFM; Pharr-Oliver model for nanoindentation), it is more likely that the large difference in modulus results from surface defects on the sample. When a certain thickness of amorphous carbon is present on the cut surface, the AFM test with a shallow indentation depth is more affected than the nanoindentation test with its deeper indentation depth. This means that the lower measured indentation modulus from AFM test corresponds to the presence of a softer layer of amorphous carbon. Meanwhile, on the cleaned surface, the AFM measured an indentation modulus of 26.32 GPa, which is consistent with that from nanoindentation, suggesting that the softer amorphous carbon was cleaned off, or reduced to a level that had a negligible effect on the indentation experiments. The three different experiments are essential to draw the above conclusion. If indentation experiments were only carried out on clean surfaces and consistent results were obtained, this could be due to the modulus of the amorphous carbon being similar to the transverse modulus of the carbon fibre, or the amorphous carbon layer is so thick that both experiments measured the amorphous carbon. The conclusion that the amorphous carbon is soft is an important point for the later discussion in paper C.

5.1.2 Indentation results and the elastic hysteresis of carbon fibres

In paper C the indentation moduli of three different carbon fibres, IMS65, T800 and M60J, were measured in two different oriented milled surfaces. The indentation moduli measured from AFM and nanoindentation for the three carbon fibres in two directions are listed in Table 4.

Table 4. The indentation moduli from AFM and nanoindentation in transvers and longitudinal directions.

Carbon fibre	Methods	Indentation modulus [GPa] in	
		transvers direction	longitudinal direction
IMS65	AFM	25.2 ± 1.2	106 ± 8
	Nanoindentation	24.6 ± 0.7	54.3 ± 1.3
T800	AFM	13.8 ± 0.6	90.5 ± 7.5
	Nanoindentation	13.7 ± 0.1	31.1 ± 0.9
M60J	AFM	17.8 ± 0.7	111 ± 15
	Nanoindentation	17.4 ± 0.3	37.5 ± 0.8

The indentation modulus in the longitudinal direction obtained by nanoindentation is much lower than the indentation modulus obtained by AFM. Since the results of both experimental methods agree in the transverse section, errors due to the different mechanical models can be excluded. On the other hand, in paper B it was proven that the modulus of amorphous carbon is lower. Therefore, it is unlikely that the high modulus measured in the AFM is caused by surface defects such as amorphous carbon. In comparison to the literature, moduli of around a few tens of GPa are often obtained using nanoindentation instruments [85, 86, 87, 88, 89]. The only available indentation results from the AFM have also yielded high moduli of around 100 GPa [90]. This is all consistent with the results reported in paper C. To select the correct indentation modulus for later model calculation, the reason for the low moduli from nanoindentation needs to be identified.

Observation of the indentation curves in the transverse section shows that the indentation depth recovers after complete unloading, yet the unloading curve is completely different from that at loading (Figure 16a). This phenomenon of purely elastic deformation but different deformation and recovery curves is referred to as hysteresis. It is very important to note that the indentation curves in literature [85-79] are also found to possess this characteristic. Unfortunately, it has not been discussed. The possible causes of this phenomenon are reversible plastic deformation [91] (Figure 16c) or nano-buckling (Figure 16b).

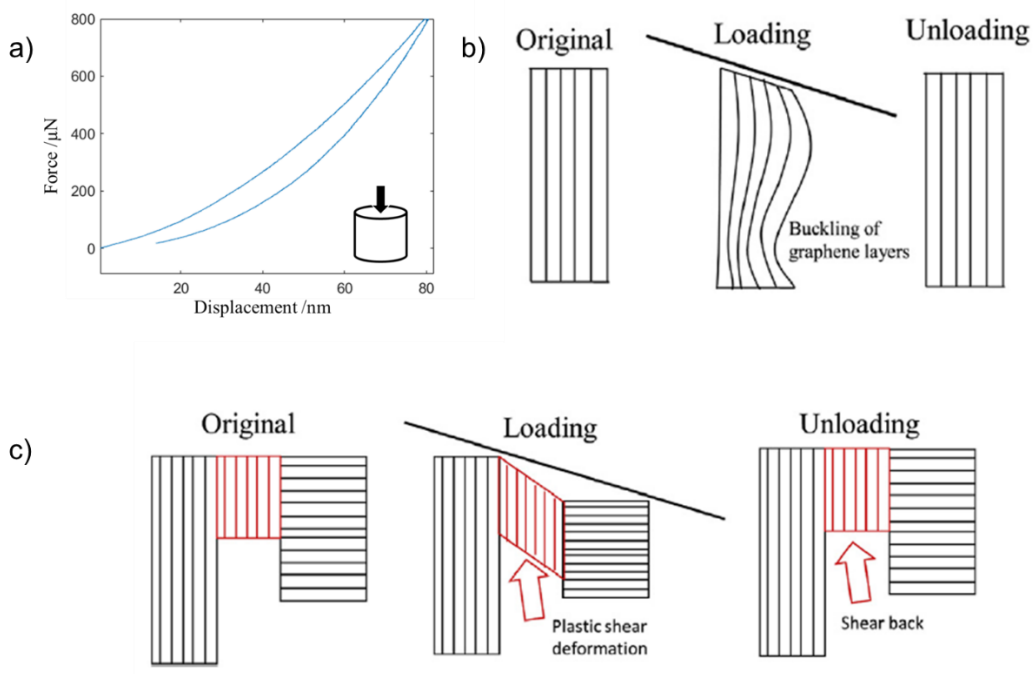

Figure 16. a) Indentation curve in longitudinal direction. Diagram of b) nano-buckling and c) reversible plastic deformation. The images are from paper C.

Reversible plastic deformation means that although plastic deformation is present during loading, the plastically deformed material is force back to its original shape by the surrounding elastic stress field during unloading. When two phases in a material exist and the yield strength of one phase is much higher than the other one, then, under the force/stress, the strong phase is only deformed elastically, while the weak phase is already deformed plastically. When the force is removed, the strong phase releases its elastic energy to deform back as shown in Fig 16c. The elastic energy is sufficient to cause the weak phase to deform plastically again to fit the geometry of the strong phase. An extreme example can be described as a porous structure. The strong phase is the solid phase, and the weak phase is the air in the pores. Assuming a condition that the overall material undergoes elastic deformation under a certain force. At this point the air phase in the pore can be seen as having undergone plastic deformation, as the air has a yield strength of zero. Since the solid phase has only been deformed elastically, it is logical that it should return to its original shape after unloaded. However, since no energy is required to change the shape of the air, there is no hysteresis phenomenon occurring. If the air is changed to other weak phase, then a hysteresis will occur. The plastic deformation of the weak phase during loading and unloading absorbs energy, therefore the unloading curve is lower than the loading curve, resulting in the elastic hysteretic response. Although there are not two phases in carbon fibre, the grain has a very strong anisotropy. Its shear modulus and strength are much lower than in the other directions. Depending on the orientation of the specific grains and the direction of the stress, some crystals can be seen as a weak phase relative to the rest of the grains.

Nano-buckling refers to the phenomenon of buckling of graphene layers as shown in Figure 16b. Before buckling, the material has a high modulus, while after the buckling has occurred, the graphene layers start to bend, and the effective modulus decreases. During unloading, the bent graphene layers will gradually return to their original shape as only elastic deformation occurs.

5.1.3 Elastic moduli of pristine carbon fibres

Both possible explanations suggest that the higher modulus at the beginning of loading curve is more in line with the corresponding elastic properties of the material itself. The unloading curves may include different deformation mechanism. Therefore, only the indentation modulus measured by the AFM is used to derive the elastic modulus of the material. By using the Swanson's model, the indentation moduli measured in each of the two different directions correspond to a relationship between E_t and G_{lt}. The two curves intersect at a point where the E_t and G_{lt} are obtained.

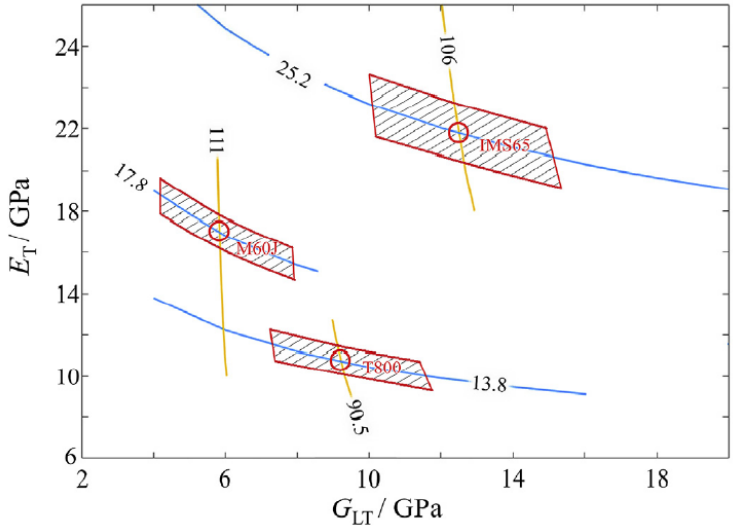

Figure 17. The transverse and shear modulus of three different carbon fibres derived from the contour map from Swanson's model. The figure is from paper C.

5.2 Characterisation of lithiated carbon fibres

Lithiated carbon fibres are carbon fibres that have been charged with lithium. In a structural battery, the charging process corresponds to the transformation of the pristine carbon fibre into a lithiated carbon fibre. With the insertion of lithium, the internal atomic structure of the carbon fibre is changed and therefore its geometrical volume and mechanical properties are also changed. This phenomenon has been observed and modelled on similar electrode materials, such as graphite and silicon [92,93]. For a structural battery, a load-bearing material, the changes in volume and mechanical properties are particularly important. This is because volume changes and mechanical property changes during cycling may cause internal damage formation, which in turn affects the mechanical integrity of the entire material [94,95]. Ideally, one can design mechanically stable structures for a structural battery by simulating the charging and discharging cycle process. A prerequisite for such simulations is the knowledge of the fundamental properties of each component. However, the properties of lithiated carbon fibres have not been fully measured, mainly due to the small size of the carbon fibres and the reactivity of lithiated carbon fibres. In paper D, lithiated carbon fibres were successfully transferred to SEM under the protection of an ionic liquid and transverse compression experiments were carried out using a hand-size nanoindenter. In addition, volume expansion of lithiated carbon fibres were studied by optical microscopy and SEM. The experimental method developed in papers B and C cannot be directly applied here because the lithiated carbon fibres will inevitably be in contact with air during the removal of the FIB/SEM milled sample from the instrument.

5.2.1 Volume change of lithiated carbon fibre

The crystal interlayer spacing, volume change and lithium capacity of the IMS65 carbon fibre at different SOC are listed in Table 5. The IMS65 carbon fibre expanded by approximately 6.6 % in diameter and 0.69 % in axial direction after the first lithiation. The results are slightly larger than the results measured by Jacques et al. [96]. After the first delithiation, the diameter and axial length were recovered. The radial expansion of the lithiated carbon fibres is mainly due to the increased graphene interlayer spacing after lithiation. This is consistent with the measured expansion of the interlayer spacing. This expansion ratio is greater than that of lithiated graphite [93]. This is due to the larger graphene interlayer spacing and weaker van der Waals attraction in the carbon fibre compared to the graphite. The weaker van der Waals attraction are not sufficient to counteract the repulsive forces between the lithium ions, resulting in the larger expansion ratio. Such situation also occurs in other similar carbon materials such as chemically reduced graphene oxide [97]. It is worth noting that approximately 25 % of the lithium remain in the carbon fibre after delithiation. These residual lithium atoms are partly in the solid electrolyte interface (SEI) and partly trapped in the carbon fibre. The trapped lithium makes the graphene interlayer spacing of delithiated carbon fibre to remain larger than the initial layer spacing. This suggests that the residual lithium may have been near the pores in the carbon fibres and therefore did not contribute to an overall volume change.

Table 5. Interlayer spacing, geometric expansion and lithium capacity of pristine, first lithiated and delithiated IMS65 carbon fibre

SOC	Interlayer spacing	Transverse expansion	Longitudinal expansion	Lithium content
Pristine	3.45 Å	-	-	0 mAh/kg
First Lithiation	3.87 Å	6.6%	0.69%	320 mAh/kg
First Delithiation	3.72 Å	-0.5%	0%	90 mAh/kg

5.2.2 Sample Transfer by ionic liquid

To perform tests on lithiated carbon fibres, the sample must be kept in a dry, oxygen-free environment. Lithiated carbon fibres exposed to air will corrode in a very short time. As shown in Figure 18a, the surface of the lithiated carbon fibre exposed to air for a minute before transfer into the SEM shows a number of cone-shaped dendrites. The indenter used to perform the compression experiments exposed the samples to air for approximately 2 to 4 minutes during sample mounting and evacuation. To protect the sample, an ionic liquid is applied to the surface of the lithiated carbon fibres. The ionic liquid is made of molten salts at room temperature. The strong ionic bonding ensures that it does not evaporate in vacuum. This is particularly important for experiments using SEMs, as the vapours generated by volatile organic solvents in vacuum of an SEM can enter into the electron column and harm the instrument. In addition, the use of ionic liquids does not cause charging effects. Although the lithiated carbon fibres are covered by the ionic liquid, the carbon fibres can still be easily positioned as shown in Figure 18b.

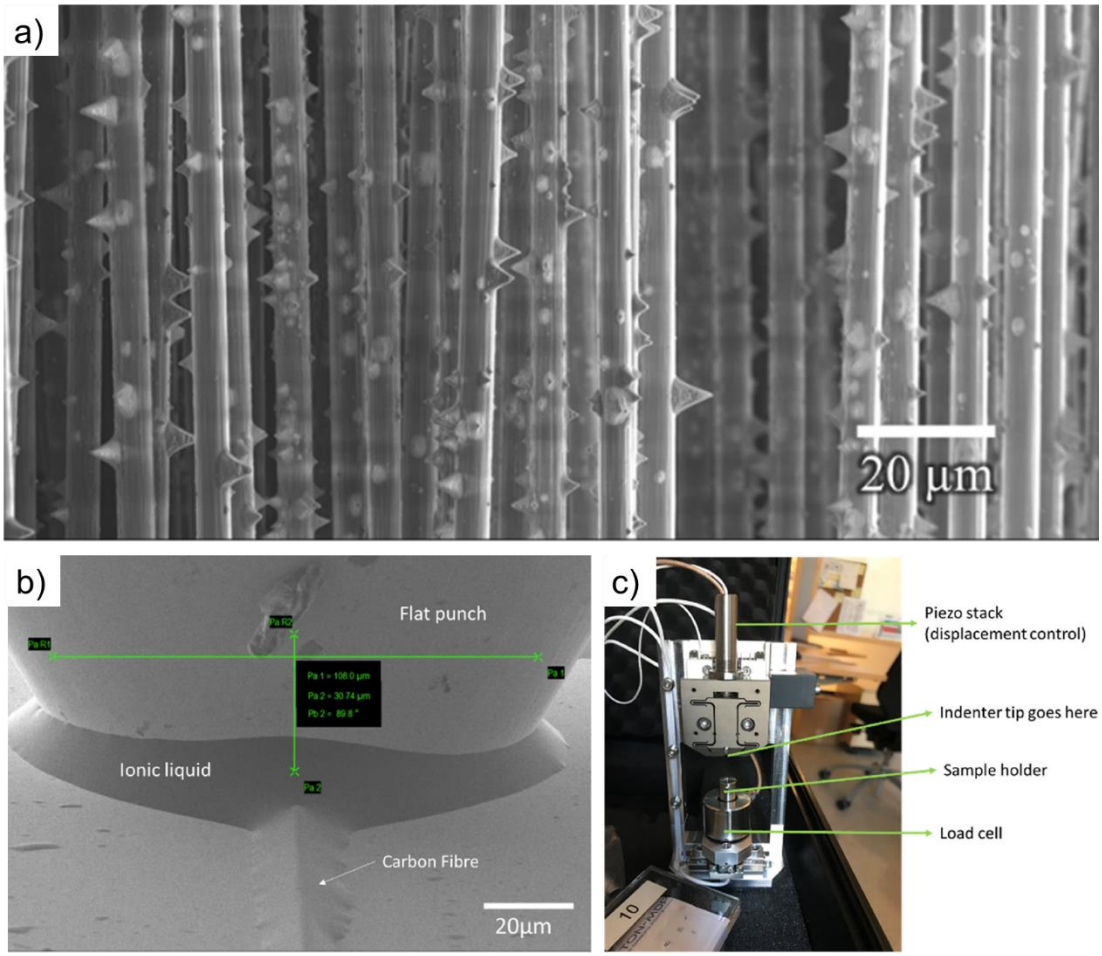

Figure 18. a) Air corrosion of carbon fibres after 1 min exposure to air, b) The lithiated carbon fibre covered by ionic liquid is ready for a compression test, c) the indenter used in the SEM. Images are from paper D.

5.2.3 Elastic model of lithiated carbon fibre

The transverse modulus of the pristine, first lithiated and first delithiated carbon fibres is presented in Table 6. After the first lithiation, the transverse modulus of the lithiated carbon fibre is 2.07 times higher than that of the pristine carbon fibre. After the lithium discharge, the modulus returned almost to that of the pristine fibre. The trend is expected. This is because the main insertion sites for lithium ions into the carbon fibre are either between graphene layers or at defects since there are more free space and energy favourable for insertion. The graphene layers are attracted to each other by the weak van der Waals bonds. Kinetic simulations show that lithium ions can either form strong covalent bonds with carbon atoms [98] or cation-pi interactions [99]. The enhanced bonding often corresponds to an increase in the elastic modulus, since the modulus is a derivation of the bonding force and a secondary derivation of the bond energy. This strengthening effect is consistent with the results of theoretical simulations of lithiation in graphite [98, 99]. At defects, the effect of lithiation on the elastic modulus has not been studied by any simulation. Theoretically, the carbon atoms at the defect are still connected by covalent bond, though the number of bonds is insufficient. The inserted lithium would form bonds with the surrounding carbon atoms. In total, the number of bonds is increased and therefore leads to an increase in modulus, but not as pronounced as the effect from interlayer lithium ions.

It is worth noting that the transverse compression modulus of 7.4 GPa measured by compression experiments is much lower than the transverse modulus of 21.8 GPa measured by indentation experiments in papers B and C. This is similar to other works in the literature. The transverse modulus measured using indentation is often higher than 10 GPa or even 20 GPa [82,84], while the transverse modulus measured from the transverse compression is lower than 10 GPa [81,100]. For T300 carbon fibre, the indentation test measured a modulus of 27.6 [82], while the compression test measured moduli of 6.05 GPa [100] and 7.79 GPa [81]. This may be related to the different deformation mechanisms at different scales. For example, in polycrystalline graphite, the more grains involved in deformation, the lower the measured modulus tends to be [101]. This may be due to the increased proportion of shear deformation in the overall deformation.

The modulus in the longitudinal direction was calculated from a constant stiffness of lithiated carbon fibres, which was reported in previous work by Jacques et al. [102] and the expansion data measure from in paper D and is listed in Table 6. The axial stiffness of the lithiated carbon fibres is constant because the number of graphene layers does not change after lithiation. The constant number of graphene planes, as the main load-bearing part, corresponds to a constant stiffness of the carbon fibre. However, as the cross section expands after lithiation, the corresponding modulus decreases.

Table 6 The elastic moduli and changing ratios of the pristine, first lithiated and first-delithiated IMS65.

SOC	Transverse direction		Longitudinal direction	
	Modulus [GPa]	Stiffening ratio	Modulus [GPa]	Stiffening ratio
Pristine	7.4	1	290	1
First Lithiation	15.3	2.07	255	0.88
First Delithiation	7.6	1.03	293	1.01

5.3 3D reconstruction of SBE

The SBE plays a role in mechanical load transfer and lithium ion transfer in a structural battery, and the properties of the SBE directly affect the properties of the entire structural battery. In paper A, although the structural battery shows an advanced multifunctionality, we still need to recognise that there is room for improvement. It is important to note that the energy density of the electrode material is not fully exploited. The electrode material showed a reduced energy capacity in the structural battery compared to a liquid battery. This is possibly because the lower ionic conductivity of the SBE compared to liquid electrolyte. The ionic conductivity of the SBE is achieved by the liquid electrolyte in a porous structure. The amount of pore, the size of pore, the morphology and especially the interconnectivity between the pores will greatly affect the ionic conductivity. To characterise the SBE, conventional 2D SEM micrographs are inadequate. For example, the SBE pores in a 2D image are often independent. Isolated pores are not capable of providing ionic conductivity. This is inconsistent with the viability of SBE in practice. This is because although the pores appear to be insulated in the 2D image, they can be interconnected in 3D space by several zigzag routes. This connectivity, or tortuosity cannot be obtained from study based on 2D images. 3D reconstruction then becomes the most feasible way to characterise the SBE. Similar characterisation of the pore structure by FIB/SEM has been shown to be feasible [103, 104, 105, 106, 107]. In paper E, the 3D structure of the SBE is

reconstructed from consecutive FIB milled surface images and simulated using the finite element method (FEM).

5.3.1 3D reconstruction and analysis of the SBE

The method of FIB/SEM milling, and reconstruction has been described in Chapter 3. An SBE with a volume of approximately 5.4×6.3×1.2 μm^3 was successfully reconstructed in 3D. The 3D model is presented in Figure 19a, where the blue colour is the polymer phase and the orange colour is the pore phase. The models are voxel-based. By 6-connected analysis, 99.3% of the pores were found to be connected. This is in line with the experimental result that the weight difference between the SBE before and after drying is almost equal to the weight of the liquid phase added at the time of fabrication. Further using the watershed method, the polymer and pore models can be broken down to consist of small individual polymers or pores. This allows to analyse the polymer and pore size distribution.

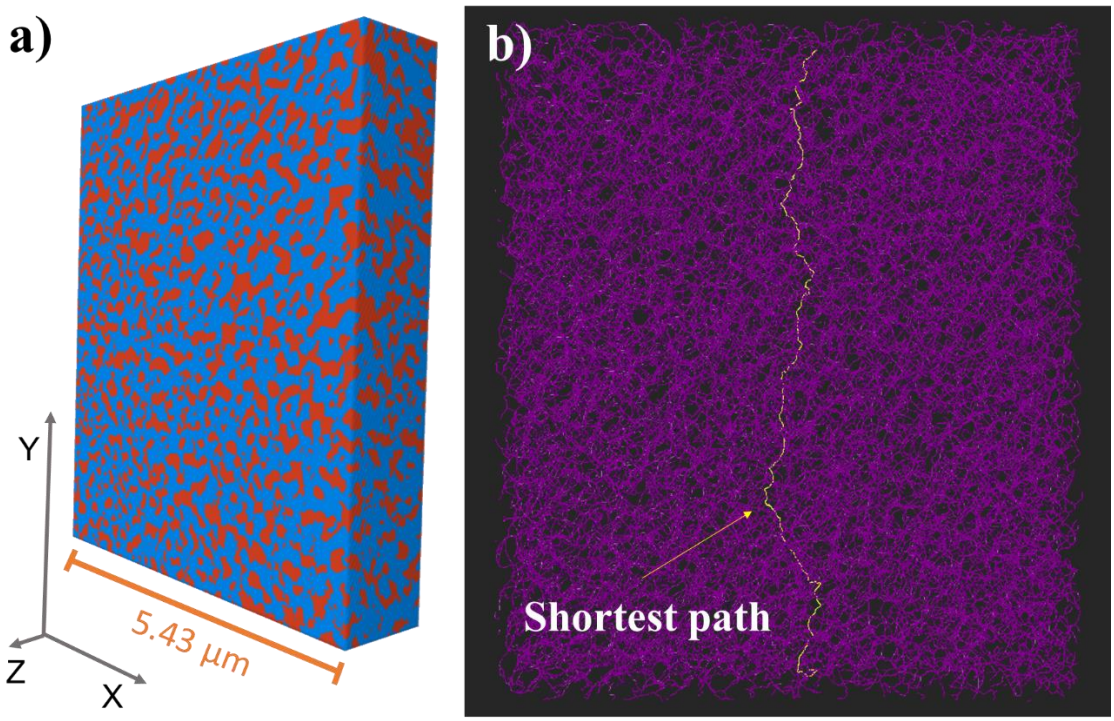

Figure 19. a) 3D reconstructed model of polymer phase (blue) and pore phase (orange). b) A shortest path in dense graph.

5.3.2 Geodesic Tortuosity

Geodesic tortuosity is defined as the ratio of the distance of the shortest path between two points to the distance of the straight line between the two points. A larger geodesic tortuosity means a longer distance for the lithium ions to travel. This often corresponds to a reduced ionic conductivity.

The 3D model of the SBE pores is transformed into a skeleton graph. A skeleton graph is a model consisting of points and edges. The points correspond to the locations of the pores and the edges correspond to the shortest paths between the pores. Compared to the 3D voxel mesh model, the skeleton diagram is easier to analyse and calculate. As shown in Figure 19b, the shortest paths between pores can be calculated in skeleton dense graph. The dense graph possesses sufficiently high resolution to accurate analyse the paths through pores. By analysing the shortest paths in the x, y and z directions, the geodesic tortuosity in the different directions

is calculated and listed in Table 7. The geodesic tortuosity is consistent in the three directions. A slightly lower tortuosity found in the z direction is due to the lower spatial resolution (20 nm) in this direction, which causes high tortuous paths to straighten. The average geodesic tortuosity is 1.8 only considering x and y directions, which means that the lithium ion must travel 80% longer distances in the SBE.

Table 7. The geodesic tortuosity of the SBE in x, y, z directions from paper E.

	Geodesic tortuosity
x-direction	1.79
y-direction	1.81
z-direction	1.72

5.3.3 Simulation vs. experiment

The 3D model of the SBE was meshed into a voxel mesh and finite element modelling (FEM) simulations were carried out in COMSOL using the modelling approach developed by Tu et al. [108]. The two target quantities for the simulations were the elastic modulus and the ionic conductivity of the SBE. These two quantities were also measured experimentally. The elastic modulus and ionic conductivity of SBE and polymers obtained from the experiments and simulations are listed in Table 8.

Table 8. The elastic modulus and lithium-ion conductivity of the bulk polymer/liquid and SBE.

	Measured	Numerical prediction
Elastic modulus [MPa]	611	738
Ionic conductivity [mS/cm]	0.134	0.633

In terms of elastic modulus, the simulated and experimental results are similar. A larger simulated modulus is expected. This is because the boundary conditions are set stricter in the FEM simulations. In terms of ionic conductivity, the simulation result overestimates the experimental result. This can arise from a number of reasons. For example, there is a certain amount of swelling in the actual SBE, which makes its pores smaller and lower porosity in the wet state [109]. In contrast, the samples reconstructed in paper E are dried SBE. The dried SBE may therefore be expected to have a higher porosity, and therefore a higher ionic conductivity than that of a swollen sample. From the simulation point of view, the model considers normal diffusion according to Fick's law only, whereas in reality there may be more effects [110], such as migration and convection.

6 Summary of appended papers

Paper A: A structural battery and its multifunctional performance

A structural battery was fabricated and characterised in paper A. The structural battery uses a carbon fibre anode, an LFP cathode, an SBE and a glass fibre separator. There are two types of glass fibre separators: micro-Glass fibre filter paper with a thickness of 185 µm and glass fibre plain weave with a thickness of 100 µm. The multifunctionality of the carbon fibre, i.e., the outstanding mechanical properties and the lithium storage capacity, has been used for the first time in a battery. This enables the structural battery with an energy density of 25 Wh/kg and a Young's modulus of 24 GPa in the direction of carbon fibre. The realisation of the battery demonstrates the feasibility of the structural battery concept and its superiority in achieving multifunctionality. In addition, the properties exhibited by the batteries prepared with two different separator thickness also show that there is high potential to improve the performance of the structural battery when a thinner separator becomes available.

Paper B: Transverse modulus measurement of carbon fibre by atomic force microscope and nanoindentation

This work focuses on the preparation of flat surfaces on carbon fibres using the FIB/SEM technique and the indentation tests by AFM and nanoindentation. The cleaning effect of using low energy Ga^+ ions on the milling surface is studied. The efficiency and necessity of the cleaning process is demonstrated by comparing the results of indentation experiments performed at different depths on uncleaned and cleaned surfaces. The modulus of the amorphous surface damage caused by FIB milling is found to be lower than that of the carbon fibre.

Paper C: Determination of transverse and shear moduli of single carbon fibres

In this paper, the transverse and shear moduli of three different structural battery carbon fibre anode candidates are measured by indentation experiments in two directions. The paper develops a complete route from sample preparation, modulus measurement, data analysis and modulus extraction. Flat surfaces on the carbon fibres were milled by FIB/SEM allowing precise control of the position and angle. The indentation experiments were carried out using nanoindentation and AFM. The data analysis of nanoindentation used a conventional method. However, as conventional AFM was not suitable for measuring hard materials, we have also developed a new calibration method using two different standard samples to eliminate the calibration errors from conventional method. In the longitudinal cross-section, the nanoindentation and the AFM give consistent results. However, in the transverse cross-section, the modulus measured by the AFM is much higher than the modulus measured by the nanoindentation. The inconsistency between the two methods is due to the hysteresis of the

carbon fibres. Two possible explanations for the hysteresis were explained. Finally, the high moduli measured by the AFM are used in subsequent modulus extraction. By fitting the indentation modulus contour map calculated using the Swanson's orthotropic contact model, each indentation modulus corresponds to a curve of the transverse and shear moduli of the carbon fibres. The transverse and shear moduli can be determined by the intersection point of the two curves corresponding to the indentation moduli in two different directions.

Paper D: Effect of lithiation on the elastic moduli of carbon fibres

In this paper, the effects of lithiation on volume and mechanical properties of carbon fibre anodes are investigated. As an important load-bearing component in the structural battery, this knowledge regarding the fibre is necessary. The volume expansion of the carbon fibres due to lithiation was found to be more pronounced in the transverse direction with an radius expansion by 6.6 %. The expansion ratio in the longitudinal direction was less than 1 %. As the lithiated carbon fibres corrode rapidly in air, a simple and convenient method was proposed and applied to successfully transfer lithiated carbon fibres into the SEM. This was to use a battery-grade hydrophobic ionic liquid to coat the lithiated carbon fibre. The ionic liquid was found to be stable in vacuum and did not affect the results of the compression experiments. Through transverse compression experiments, the lithiated carbon fibres were found to have more than double the transverse modulus than the pristine fibres. The stiffening effect was also restored after delithiation. In the longitudinal direction, a softening effect on the modulus was found due to the significant cross-sectional expansion and the constant stiffness of the carbon fibre. The knowledge can be used in micro-scale simulations of a structural battery to design stable structures under charging / discharging cycles.

Paper E: 3D reconstruction and computational analysis of a porous polymer electrolyte matrix material for structural battery composites

In this paper, the 3D geometry of an SBE is reconstructed, analysed and simulated. SBE is the lithium-ion conductor and force transmitter in a structural battery. It is a porous structure consisting of pores of a few tens to hundreds of nanometres. A 3D model of the SBE has been successfully reconstructed from slicing images obtained using continuous FIB/SEM milling technique. The interconnectivity, diameter and volume distribution of the pores were obtained. Approximately 99.3% of the pores were found to be interconnected. The pore models were transformed into skeleton graphs and the shortest path distances between the different pores were calculated. The geodesic tortuosity in the x, y, and z-directions was calculated and found to be approximately 1.8, and material isotropy was confirmed. The model was meshed and the elastic modulus and ionic conductivity of the SBE were computed using COMSOL. The predicted elastic modulus was in good agreement with the experimentally measured value, while the simulated ionic conductivity was much higher than the experimentally measured value. Reasons for this discrepancy are discussed.

7 Outlook

Structural batteries have made a good start and proved their feasibility as a multifunctional new energy storage solution. Existing studies have provided part of the knowledge for the development of structural batteries. In the future, with better designs, more advanced manufacturing methods and a better knowledge of materials, practical structural batteries can be expected to be made and successfully used in various applications, such as in electric vehicles. In the author's experience, structural batteries and related characterisation can be investigated in more depth in the following areas.

7.1 Structural battery

7.1.1 Thin separator

In current practice, the diaphragms used in structural cells are glass fibre filter paper and glass fibre woven fabric. These are much thicker than the current commercial lithium-ion battery separators, which range from 10 to 25 μm. In the attempts that have been made, the results with commercial separators have not been satisfactory, which causes a reduction in the total capacity of the battery. However, the overall reduction in battery weight due to thin separators is significant. A suitably thin separator will significantly increase the energy density and the modulus of a structural battery. Suitable separators should have characteristics such as thin thickness, high porosity and small pores. Of these, high porosity and thin thickness are often traded-off in relation to each other. As the first step, optimising this relationship using both the experiment and simulation method can help to find a better separator.

7.1.2 Manufacturing process

The published structural batteries are made using hand lay-up. This leads to some manual errors. For example, the carbon fibres are not aligned properly, they are not evenly distributed and there may be dry spots inside the battery. These can reduce the overall performance of the structural battery. In a very recent master thesis, it has been found that the use of standard vacuum infusion method can solve these problems to a large extent [111]. Vacuum infusion as a common production process for making carbon fibre reinforced composites that allows for manufacture of different shapes. Structural batteries may also need to be used in non-planar applications. It is interesting and of practical importance to be able to produce more complex structural batteries such as curved shapes.

7.1.3 Fabrication of a multi-layer structural battery

Current structural batteries have only one layer of anode, one layer of cathode and one layer of separator. The total energy capacity of a single layered structural battery is therefore not enough for most practical applications. To expand the structural battery to possess sufficient capacity to meet practical requirements, multiple layers are necessary. Extending the vacuum infusion

method for multilayer structural batteries may cause new problems, such as insufficient interlayer SBE and interlayer pressure. These problems can be addressed after a suitable separator is found.

7.1.4 Different battery structures

Lithium-ion battery can be built by different types of structure, i.e., cylindrical batteries, coin cells, prismatic batteries and pouch cells. The current structure battery only uses the pouch battery structure. However, in the field of electric vehicles, cylindrical and prismatic batteries are the most used. The different configurations of batteries have their own advantages, for example cylindrical batteries are cheaper to produce and prismatic batteries are more space efficient. The development and production of structural batteries with different structures is important for the practical application.

7.2 Characterisation of structural battery materials

7.2.1 Characterisation of carbon fibres after multiple cycles

Work has been done to develop methods for characterising carbon fibre anodes in structural batteries and to measure the first lithiation and delithiation of carbon fibres. In practice, batteries are charged and discharged for thousands of cycles. After long periods of charge and discharge, the electrode material commonly undergoes different level of degradation. The slow degradation of the carbon fibre anode may extend the lifetime of the structural battery. It is necessary to characterise the carbon fibre anode after many cycles using established methods.

7.2.2 Characterisation of LFP-coated cathodes

LFP-coated cathodes are under development as the eventual cathode material for structural batteries [112, 113]. For example, Sanchez et al. use electrophoretic deposition to make LFP-plated cathodes that can be used in liquid batteries [112, 113]. The use of such cathode materials in structural batteries is not ready. In the future when a usable cathode material is made. Its mechanical properties can be tested at the micro-scale.

7.2.3 Characterisation of SBE in structural batteries

SBE alone has been successfully reconstructed using FIB/SEM. SBE is produced by a phase separation method. Therefore, the polymerisation rate of the solid phase will determine the morphology of the SBE. In a structural battery, the SBE is present inside the separator, between carbon fibres anode and cathode particles. A large number of solid surfaces are present in each of these locations. Since polymerisation tends to occur on the free surface first, the high specific surface area inside the structural battery is likely to affect the phase separation process of the SBE. This may cause the morphology of SBE in or on the surfaces of the separator, anode and cathode to be different from that of pure SBE. For example, when using different separators, the morphology of the SBE may be influenced by the material of the separator and the size of the pores. As most commercial separators are only 40-50 % porous with sub-microscale pores. When the SBE is cured in the separator, the overall porosity becomes even smaller, and the pore size can also be affected. This results in the SBE-cured separator becoming a bottleneck for ionic conduction. This can be investigated by 3D reconstruction, analysis and simulation of the SBE-cured separator using a process that has been developed. On the other hand, when solid electrolytes are used, the interface resistance tends to be high. In addition, the carbon fibre anode has been found to have repeated volume changes during the charge/discharge cycle of about 6.6% in the radial direction. This can lead to cracks or detachment at the interface between the SBE and the carbon fibre anode. Therefore, not only the interface between the SBE

and the electrode in the initial state is worth investigating, but also the interface after repeated charging/discharging cycles.

7.2.4 Study of SBE in cryo-SEM

The existing work has performed FIB/SEM cuts and 3D reconstructions of the SBE. It is important to note that the studied SBE sample was dried in vacuum. The dried SBE may have a different morphology to that in the wet state. For example, in the wet state, the polymer skeleton can absorb some liquid electrolyte and swell. This results in a lower porosity, smaller pore size and less liquid electrolyte content. Using cryo-SEM, a wet SBE can be directly studied in a frozen state, which provides measurements of the SBE under more realistic condition.

References

[1] T. Kim, W. Song, D. Son, L.K. Ono, Y. Qi, Lithium-ion batteries: outlook on present, future, and hybridized technologies, *Journal of Materials Chemistry A*, 2019, 7, 2942-2964.

[2] X. Bing, R. Zhang, C. Zhao, Q. Zhang, Toward Safe Lithium Metal Anode in Rechargeable Batteries: A Review, *Chemical Reviews*, 2017, 117, 15, 10403–10473.

[3] X. Zuo, J. Zhu, P. Müller-Buschbaum, Y. Cheng, Silicon based lithium-ion battery anodes: A chronicle perspective review, *Nano Energy*, 2017, 31, 113-143.

[4] L. Song, J. Du, Z. Xiao, P. Jiang, Z. Cao, H. Zhu, Research Progress on the Surface of High-Nickel Nickel–Cobalt–Manganese Ternary Cathode Materials: A Mini Review, *Frontiers in Chemistry*, 2020, 8, 761.

[5] Q. Zhao, S. Stalin, C. Zhao, L.A. Archer, Designing solid-state electrolytes for safe, energy-dense batteries, *Nature Reviews Materials*, 2020, 5, 229-252.

[6] S. Kalnaus, L.E. Asp, J. Li, G.M. Veith, J. Nanda, C. Daniel, X. Chen, A. Westover, N.J. Dudney, Multifunctional approaches for safe structural batteries, *Journal of Energy Storage*, 2021, 40, 102747.

[7] L.E. Asp, S. Greenhalgh, Structural Power Composites, *Composites Science and Technology*, 2014, 101, 41-61.

[8] L.E. Asp, M. Johansson, G. Lindbergh, J. Xu, D. Zenkert, Structural battery composites: a review, *Functional Composites and Structures*, 2019, 1, 042001.

[9] W. Johannisson, N. Ihrner, D. Zenkert, M. Johansson, D. Carlstedt, L.E. Asp, F. Sieland, Multifunctional performance of a carbon fiber UD lamina electrode for structural batteries, *Composites Science and Technology*, 2018, 168, 81-87.

[10] F. Mo, G. Liang, Z. Huang, H. Li, D. Wang, C. Zhi, An Overview of Fiber-Shaped Batteries with a Focus on Multifunctionality, Scalability, and Technical Difficulties, *Advanced Materials*, 2019, 32, 1902151.

[11] B.A. Newcomb, Processing, structure, and properties of carbon fibers, *Composites Part A*, 2016, 91, 262.

[12] Y. Liu, B. Zwingmann, M. Schlaich, Carbon Fiber Reinforced Polymer for Cable Structures—A Review, *Polymers*, 2015, 7, 2078-2099.

[13] M.H. Kjell, E. Jacques, D. Zenkert, M. Behm, G. Lindbergh, PAN-Based Carbon Fiber Negative Electrodes for Structural Lithium-Ion Batteries, *Journal of The Electrochemical Society*, 2011, 158, 1455.

[14] D. Carlstedt, L.E. Asp, Performance analysis framework for structural battery composites in electric vehicles, *Composite Part B*, 2020, 186, 107822.

[15] J.B. Donnet, T.K Wang, J. Peng, S. Rebouillat, *Carbon Fibers*, Marcel Dekker, 3rd edition, 1998.

[16] J. R. Dahn, T. Zheng, Y. Liu, J. S. Xue, Mechanisms for Lithium Insertion in Carbonaceous Materials, *Science*, 1995, 270, 590.

[17] G. Fredi et al., Graphitic microstructure and performance of carbon fibre Li-ion structural battery electrodes, *Multifunctional Materials*, 2018, 1, 015003.

[18] M. Endo et al., In situ Raman study of PPP-based disordered carbon as an anode in a Li ion battery, *Synthetic Metals*, 1998, 98, 17–24.

[19] M. Endo, A. Kim, *Applications of advanced carbon materials to the lithium ion secondary battery Carbon Alloys*, Oxford: Elsevier Science Ltd, 2003, ch 25.

[20] J. Hagberg, S. Leijonmarck, G. Lindbergh, High precision coulometry of commercial PAN-based carbon fibres as electrodes in structural batteries, *Journal of The Electrochemical Society*, 2016, 163 A, 1790–6.

[21] K. Xu, Nonaqueous Liquid Electrolytes for Lithium-Based Rechargeable Batteries, *Chemical Reviews*, 2004, 104, 4303- 4418.

[22] J.F. Snyder, R.H. Carter, E. D. Wetzel, Electrochemical and Mechanical Behavior in Mechanically Robust Solid Polymer Electrolytes for Use in Multifunctional Structural Batteries, *Chemistry of Materials*, 2007, 19 (15), 3793−3801.
[23] N. Ihrner, W. Johannisson,F. Sieland, D. Zenkert, M. Johansson, Structural lithium ion battery electrolytes via reaction induced phase-separation, *Journal of Materials Chemistry A*, 2017, 5, 25652.
[24] L.M. Schneider, N. Ihrner, D. Zenkert, M. Johansson, Bicontinuous Electrolytes via Thermally Initiated Polymerization for Structural Lithium Ion Batteries, *ACS Applied Energy Materials*, 2019, 2 (6), 4362.
[25] E.D. Wetzel, Reducing weight: Multifunctional composites integrate power, communications, and structure, *AMTIAC Quarterly*, 2004, 8, 91-95.
[26] E. L. Wong et al., Design and Processing of Structural Composite Batteries. *In Proceedings of Society for the Advancement of Materiel and Process Engineering* (SAMPE) 2007, 3–7.
[27] P. Liu, E. Sherman, A. Jacobsen, Design and fabrication of multifunctional structural batteries, *Journal of Power Sources*, 2009, 189, 646-650.
[28] K. Moyer et al. Carbon fiber reinforced structural lithium-ion battery composite: Multifunctional power integration for CubeSats, *Energy Storage Materials*, 2020, 4, 676.
[29] K.D. Vernon-Parry, Scanning electron microscopy: an introduction, *III-Vs Review*, 2000, 13, 40-44.
[30] C.W. Oatley, W.C. Nixon, R.F.W. Pease: Scanning Electron Microscopy, *Advances in Electronics and Electron Physics*, 1995, 21, 181.
[31] J. Sikorski et al, A new preparation technique for examination of polymers in the scanning electron microscope, *Journal of Physics E: Scientific Instruments*, 1968, 1, 29.
[32] P. Cross, J. Hearle, B. Lomas, J. Sparrow, *froc. 3rd Symp. on Scanning Electron Microscopy* (Chicago: IIT Research Institute) 1970, 81-8.
[33] N.I. Kato, Reducing focused ion beam damage to transmission electron microscopy samples, *Journal of Electron Microscopy*, 2004, 53, 451–458.
[34] R.M. Langford, A.K. Petford-Long, Preparation of transmission electron microscopy cross-section specimens using focused ion beam milling, *Journal of Vacuum Science & Technology A*, 2001, 19, 2186.
[35] Langford R M, Focused ion beams techniques for nanomaterials characterization, *Microscopy Research and Technique*, 2006, 69, 538–49.
[36] K. Sloyan et al., A review of focused ion beam applications in optical fibers, *Nanotechnology*, 2021, 32, 472004.
[37] L.A. Giannuzzi, F.A. Stevie, *Introduction to focused ion beams: Instrumentation, theory, techniques and practise*. USA: Springer, 2005.
[38] L.A. Giannuzzi, R. Geurts, J. Ringnalda, 2 keV Ga^+ FIB Milling for Reducing Amorphous Damage in Silicon, *Microscopy and Microanalysis*, 2005, 11, 828.
[39] J. Mayer, L.A. Giannuzzi, T. Kamino, J. Michael, TEM Sample Preparation and FIB-Induced Damage, *MRS Bulletin*, 2007, 32, 400.
[40] S. Rubanov, P. Munroe, S. Prawer, D.N. Jamieson, Surface damage in silicon after 30 KeV Ga FIB fabrication, *Microscopy and Microanalysis*, 2009, 9, 884-885.
[41] K. Thompson, B. Gorman, D.J. Larson, B. van Leer, L. Hong, Minimization of Ga induced FIB damage using low energy clean-up, *Microscopy and Microanalysis*, 2006, 12, 1736-1737.
[42] L.A. Giannuzzi, F.A. Stevie, A review of focused ion beam milling techniques for TEM sample preparation, *Microscopy and Microanalysis*, 1999, 30, 197–204.
[43] H.J. Lemmens, A.R. Butcher, P.W.S.K Botha, FIB/SEM and SEM/EDX: a new dawn for the SEM in the core lab? *Petrophysics*, 2011, 52, 452–456.

[44] B. W. Kempshall et al., Ion channeling effects on the focused ion beam milling of Cu, *Journal of Vacuum Science & Technology B*, 2001, 19, 749.
[45] P.R. Munroe, The application of focused ion beam microscopy in the material sciences, *Materials Characterization*, 2009, 60, 2.
[46] S. Rubanov, P.R. Munroe, The application of FIB milling for specimen preparation from crystalline germanium, *Micron*, 2004, 35, 549.
[47] T. Ishitani, K. Umemura, T. Ohnishi, T. Yaguchi, T. Kamino, Improvements in performance of focused ion beam cross-sectioning: aspects of ion-sample interaction, *Journal of Electron Microscopy*, 2004, 53, 443.
[48] T.H. Loeber, B. Laegel, S. Wolff, Reducing curtaining effects in FIB/SEM applications by a goniometer stage and an image processing method, *Journal of Vacuum Science & Technology B*, 2017, 35, 06GK01.
[49] S. Liu, L. Sun, J. Gao, K. Li, A fast curtain-removal method for 3D FIB-SEM images of heterogeneous minerals, *Journal of Microscopy*, 2018, 272, 3.
[50] J.H. Fitschen, J. Ma, S. Schuff, Removal of curtaining effects by a variational model with directional forward differences, *Computer Vision and Image Understanding*, 2017, 155, 24-32.
[51] G. Binnig, C.F. Quate, Ch. Gerber, Atomic Force Microscope, *Physical Review Letters*, 1986, 56, 930.
[52] N. Jalili, K. Laxminarayana, A review of atomic force microscopy imaging systems: application to molecular metrology and biological sciences, *Mechatronics*, 2004, 14, 907–945.
[53] A. Brugues et al., Forces driving epithelial wound healing, *Nature Physics*, 2014, 10, 683–690.
[54] N.I. Petridou, Z. Spiró, C.P. Heisenberg, Multiscale force sensing in development, *Nature Cell Biology*, 2017, 19, 581.
[55] W. J. Tyler, The mechanobiology of brain function, *Nature Reviews Neuroscience*, 2012, 13, 867–878.
[56] J. Crest, A. Diz-Muñoz, D. Chen, D. A. Fletcher, D. Bilder, Organ sculpting by patterned extracellular matrix stiffness. *eLife*, 2017, 6, e24958.
[57] O. Marti, B. Drake, P. K. Hansma, Atomic force microscopy of liquid-covered surfaces: Atomic resolution images, *Applied Physics Letters*, 1987, 51, 484.
[58] R. Gahlin, S. Jacobson, Novel method to map and quantify wear on a micro-scale, *Wear*, 1998, 222, 93-102.
[59] R. Kaneko, T. Miyamoto, Y. Andoh, E. Hamada, Microwear, *Thin Solid Films*, 1996, 273, 105-111.
[60] K. Miyahara, N. Nagashima, T. Ohmura, S. Matsuoka, Evaluation of mechanical properties in nanometer scale using AFM-based nanoindentation tester, *Nanostructured Materials*, 1999, 12, 1049.
[61] S. Sundararajan, B. Bhushan, Development of a continuous microscratch technique in an atomic force microscope and its application to study scratch resistance of ultrathin hard amorphous carbon coatings, *Journal of Materials Research*, 2011, 16, 437.
[62] X. Li, B. Bhushan, A Review of Nanoindentation Continuous Stiffness Measurement Technique and Its Applications, *Materials Characterization*, 2002, 48 (1), 11-36.
[63] S. I. Bulychev et al., Determination of the Young Modulus from the Indentation Diagram, *Zavod. Lab.*, 1975, 41, 1137–1141.
[64] W.C. Oliver, G.M. Pharr, An improved technique for determining hardness and elastic modulus using load and displacement sensing indentation experiments, *Journal of Materials Research*, 1992, 7 (6), 1564-83.
[65] H. Hertz, Über die Berührung fester elastischer Körper, J. *für die Reine Angewandte Math.* (Crelle's J.), 1881, 92, 156-171.

[66] D.W. Hadley, I.M. Ward, J. Ward, The transverse compression of anisotropic fibre monofilaments, *Proceedings of the Royal Society of London*, 1965, 285, 275-286.
[67] P.R. Pinnock, I.M. Ward, J.M. Wolfe, The compression of anisotropic fibre monofilaments. II, *Proceedings of the Royal Society of London*, 1966, 291, 267-278.
[68] S.A. Jawad, I.M. Ward, The transverse compression of oriented nylon and polyethylene extrudates, *Journal of Materials Science*, 1978, 13, 1381-1387.
[69] S. Kawabata, Measurement of the transverse mechanical properties of high-performance fibres, *The Journal of The Textile Institute*, 1990, 81, 432-447.
[70] K. Naito, Y. Tanaka, J. Yang, Transverse compressive properties of polyacrylonitrile (PAN)-based and pitch-based single carbon fibers, *Carbon*, 2017, 118, 168-183.
[71] S.R. Swanson, Hertzian contact of orthotropic materials, *International Journal of Solids and Structures*, 2004, 41, 1945-1959.
[72] S. Duan, Characterization of elastic moduli of single fibres, *Licentiate thesis*, Chalmers University of Technology, Gothenburg, Sweden, 2020.
[73] S.-W. W. Chen, J.-L. Pellequer, DeStripe: frequency-based algorithm for removing stripe noises from AFM images, *BMC Structural Biology*, 2011, 11, 1–10.
[74] J. Chen, Y. Shao, H. Guo, W. Wang, B. Zhu, Destriping CMODIS data by power filtering, IEEE Transactions on Geoscience and Remote Sensing, 2003, 41, 2119–2124.
[75] J. Torres, S.O. Infante, Wavelet analysis for the elimination of striping noise in satellite images, *Optical Engineering*, 2001, 40, 1309–1315.
[76] B. Münch, P. Trtik, F. Marone, M. Stampanoni, Stripe and ring artifact removal with combined wavelet — Fourier filtering, *Optics Express*, 2009, 17, 8567.
[77] R. Maurin, P. Davies, N. Baral, C. Baley, Transverse properties of carbon fibres by nano-indentation and micro-mechanics, *Applied Composite Materials*, 2008, 15, 61-73.
[78] H. Miyagawa, T. Mase, C. Sato, E. Drown, L.T. Drzal, K. Ikegami, Comparison of experimental and theoretical transverse elastic modulus of carbon fibers, *Carbon*, 2006, 44, 2008.
[79] D. Mounier, V. Poilâne, C. Bûcher, P. Picart, Evaluation of transverse elastic properties of fibers used in composite materials by laser resonant ultrasound spectroscopy, *Proceedings of the Acoustics 2012 Nantes Conference*, France, 2012.
[80] K. Fujita, Y. Sawada, Y. Nakanishi, Effect of cross-sectional textures on transverse compressive properties of Pitch-based carbon fibers, *Materials Science Research International*, 2001, 7, 116-121.
[81] K. Naito, Y. Tanaka, J.M. Yang, Transverse compressive properties of polyacrylonitrile (PAN)-based and pitch-based single carbon fibers, *Carbon*, 2017, 118, 168-183.
[82] T. Csanádi, D. Németh, C. Zhang, J. Duszaac, Nanoindentation derived elastic constants of carbon fibres and their nanostructural based predictions, *Carbon*, 2017, 119, 314-325.
[83] A. Delafargue, F.J. Ulm, Explicit approximations of the indentation modulus of elastically orthotropic solids for conical indenters, *International Journal of Solids and Structures*, 2004, 41, 7351-7360.
[84] T.S. Guruprasad, V. Keryvin, L. Charleux, J.-P. Guin, O. Arnould, On the determination of the elastic constants of carbon fibres by nanoindentation tests, *Carbon*, 2021, 173, 572-586.
[85] S. Ozcan, J. Tezcan, P. Filip, Microstructure and elastic properties of individual components of C/C composites, *Carbon*, 2009, 47, 3403-3414.
[86] P. Diss, J. Lamon, L. Carpentier, J.L. Loubet, P.H. Kapsa, Sharp indentation behavior of carbon/carbon composites and varieties of carbon, *Carbon*, 2002, 40, 2567-2579.
[87] D.T. Marx, L. Riester, Mechanical properties of carbon—carbon composite components determined using nanoindentation, *Carbon*, 1999, 37, 1679-1684.
[88] M. Kanari, K. Tanaka, S. Baba, M. Eto, Nanoindentation behavior of a two-dimensional carbon-carbon composite for nuclear applications, *Carbon*, 1997, 35, 1429-1437.

[89] A. Leatherbarrow, H. Wu, Mechanical behaviour of the constituents inside carbon-fibre/carbon-silicon carbide composites characterised by nano-indentation, *Journal of the European Ceramic Society*, 2012, 32, 579-588.
[90] H. Wang et al., Stress dependence of indentation modulus for carbon fiber in polymer composite, *Science and Technology of Advanced Materials*, 2019, 20, 412-420.
[91] H. Lilholt, R. Talreja, Fatigue and Creep of Composite Materials, *The Third Risø International Symposium On Metallurgy and Materials Science*, At Roskilde, Denmark, 1982, 6-10.
[92] L. Christensen, M.N. Obrovac, Structural changes in silicon anodes during lithium insertion/Extraction, *Electrochemical and Solid State Letters*, 2004, 7, A93-96.
[93] S. Schweidler, et al., Volume changes of graphite anodes revisited: a combined operando X-ray diffraction and in situ pressure analysis study, *The Journal of Physical Chemistry C*, 2018, 122, 8829-8835.
[94] J. Xu, J. Varna, Matrix and interface microcracking in carbon fibre/polymer structural micro-battery, *Journal of Composite Materials*, 2019, 53, 3615-3628.
[95] D. Carlstedt, K. Runesson, F. Larsson, J. Xu, L.E. Asp, Electro-chemo-mechanically coupled computational modelling of structural batteries, *Multifunctional Materials*, 2020, 3, 045002.
[96] E. Jacques, M.H. Kjell, D. Zenkert, G. Lindbergh, M. Behm, Expansion of carbon fibres induced by lithium intercalation for structural electrode applications, *Carbon*, 2013, 59, 246-254.
[97] Y. Sun, et al., Comparison of reduction products from graphite oxide and graphene oxide for anode applications in lithium-ion batteries and sodium ion batteries, *Nanoscale*, 2017, 9, 2585-2595.
[98] K.R. Kganyago, P.E. Ngoepe, Structural and electronic properties of lithium intercalated graphite LiC6, *Physical Review B*, 2003, 68, 205111.
[99] Y. Qi, et al., Threefold increase in the Young's modulus of graphite negative electrode during lithium intercalation, *Journal of The Electrochemical Society*, 2010, 157, A558-A566.
[100] S. Kawabata, Measurement of the transverse mechanical properties of high-performance fibres, *The Journal of The Textile Institute*, 1990, 81, 432-447.
[101] A. Mukhopadhyay et al., thin film graphite electrodes with low stress generation during Li-intercalation, *Carbon*, 2011, 49, 2742-2749.
[102] E. Jacques et al., Impact of electrochemical cycling on the tensile properties of carbon fibres for structural lithium-ion composite batteries, *Composites Science and Technology*, 2012, 72, 792-798.
[103] Joos J. et al., Reconstruction of porous electrodes by FIB/SEM for detailed microstructure modelling, *Journal of Power Sources*, 2011, 196, 7302-7307.
[104] L. Holzer, F. Indutnyi, P.H. Gasser, B. Münch, M. Wegmann, Three-dimensional analysis of porous BaTiO3 ceramics using FIB nanotomography, *Journal of Microscopy*, 2004, 216, 84-95.
[105] N. Bassim, K. Scott, L.A. Giannuzzi, Recent advances in focused ion beam technology and applications, *MRS Bulletin*, 2014, 39, 317–325.
[106] C.Fager et al., 3D high spatial resolution visualisation and quantification of interconnectivity in polymer films, *International Journal of Pharmaceutics*, 2020, 587, 119622.
[107] C. Fager et al., Optimization of FIB-SEM Tomography and Reconstruction for Soft, Porous, and Poorly Conducting Materials, *Microscopy and Microanalysis*, 2020, 26, 837–845.
[108] V. Tu, L. E. Asp, N. Shirshova, F. Larsson, K. Runesson, R. Jänicke, Performance of bicontinuous structural electrolytes, *Multifunctional Materials*, 2020, 3, 025001.

[109] A. Sienkiewicz, P. Krasucka, B. Charmas, W. Stefaniak, J. Goworek, Swelling effects in cross-linked polymers by thermogravimetry, *Journal of Thermal Analysis and Calorimetry volume*, 2017, 130, 85–93.
[110] B. Boz, T. Dev, A. Salvadori, J.L. Schaefer, Review—Electrolyte and Electrode Designs for Enhanced Ion Transport Properties to Enable High Performance Lithium Batteries, *Journal of The Electrochemical Society*, 2021, 168, 090501.
[111] T. Samia, S. Mohammad, Improvements in structural battery cells processing: manufacture, characterization, and multicell demonstration, *Master thesis*, Chalmers University of Technology, Gothenburg, Sweden, 2022.
[112] J.S. Sanchez, J. Xu, Z. Xia, J. Sun, L.E. Asp, V. Palermo, Electrophoretic coating of LiFePO4/Graphene oxide on carbon fibers as cathode electrodes for structural lithium ion batteries, *Composites Science and Technology*,2021, 208, 108768.
[113] J. Hagberg et al., Lithium iron phosphate coated carbon fiber electrodes for structural lithium ion batteries, *Composites Science and Technology*, 2018, 162, 235.